

Laser Action in a Gas Condensation in the Vicinity of a Hot Star¹

S. Johansson* and V. S. Letokhov**

* Lund Observatory, Lund University, 221 00 Lund, Sweden

** Institute of Spectroscopy, Russian Academy of Sciences, Troitsk, Moscow region, 142190 Russia

Received April 16, 2002

In the region near 1 μm , we have found laser action in a quantum transition between highly excited states of Fe II, with its higher levels being optically pumped by the intense H Ly α radiation (1215 Å) formed in the ionized HII region of a gas condensation (blob B) in the close vicinity of the central star in η Carinae. © 2002 MAIK “Nauka/Interperiodica”.

PACS numbers: 97.10.Fy; 98.38.Hv; 95.85.Kr

Following the discovery of space microwave masers operating in the OH radicals [1] and H₂O molecules [2], such masers were found to be operative in more than 100 molecular species [3], as well as in highly excited hydrogen atoms [4] in the submillimeter wavelength region. In the IR region of the spectrum, the effect of stimulated emission of radiation in the CO₂ molecule was discovered in the Martian and Venus atmospheres [5, 6]. In this letter, we report on the laser action in the optical region of the spectrum—a possibility that was discussed as far back as 1972 [7].

The probability of finding a laser effect in the optical region differs considerably from that in the microwave region, as a result of the enormous difference (10^{15} to 10^{18} times) between the spontaneous emission rates and inverse population production mechanisms in the two wavelength regions. This follows from simple qualitative considerations of the steady-state saturation regime of the isotropic maser/laser action.

The stimulated emission of radiation in a space maser occurs as a result of pumping the upper maser level, which is not associated with spontaneous emission in microwave radiative transitions. It may therefore have a decay rate much in excess of the spontaneous emission rate, which lies in the region $A_{mn} \cong 10^{-9}$ – 10^{-7} s⁻¹. Therefore, the intensity of stimulated radiation can be many orders of magnitude higher than the intensity of spontaneous radiation, and it is only limited by the pumping rate. This is exactly the reason why the brightness temperature of maser microwave lines reaches as high a value as 10^{10} – 10^{15} K. The intensity of maser lines is not borrowed from other microwave spectral lines, which are very weak, but from other pumping sources.

In the optical region of the spectrum, the rate of allowed spontaneous transitions is high ($A_{mn} \cong 10^8$ – 10^9 s⁻¹), and it is precisely spontaneous transitions that provide the pumping of the upper level in an optical space laser at a sufficiently high rate to exceed the rates of collisional pumping mechanisms. This is especially true for the case considered here, where the space laser is indirectly pumped by H Ly α in the vicinity of η Car, one of the most luminous stars of our Galaxy. Therefore, the intensity of the stimulated radiation in the optical region generated by the occurrence of an inversion population and significant amplification cannot exceed in the steady-state regime to any substantial extent the intensity of the pumping spectral lines formed by spontaneous emission in allowed radiative transitions of atoms or ions. This fact presents difficulties in detecting laser action by a large enhancement of the radiation intensity, but it should manifest itself in comparatively moderate changes of the branching ratios of spectral lines, having a common source of pumping.

One exception is the case of quantum transitions having a relatively low spontaneous emission probability ($A_{mn} \cong 1$ – 10^5 s⁻¹), and, consequently, the spontaneous radiation lines are weak. Once an inverted level population has developed in such a transition with a significant amplification in a properly sized cloud, a stimulated emission channel opens up. The stimulated transition rate cannot be much higher than the spontaneous emission rate, which is limited by the pumping rate of the upper laser level. Thus, the intensity of the laser line should become comparable with the intensity of the lines which are due to the allowed spontaneous emission of radiation and resulting from the optical pumping (direct or indirect) of the upper level. This takes place only in the inverted population volume with size $L \gg 1/\alpha$, where α is the amplification coefficient per unit length. In such a case, a spectral line, expected to be weak, must appear as a spectral line of normal

¹ This work was submitted by the authors in English.

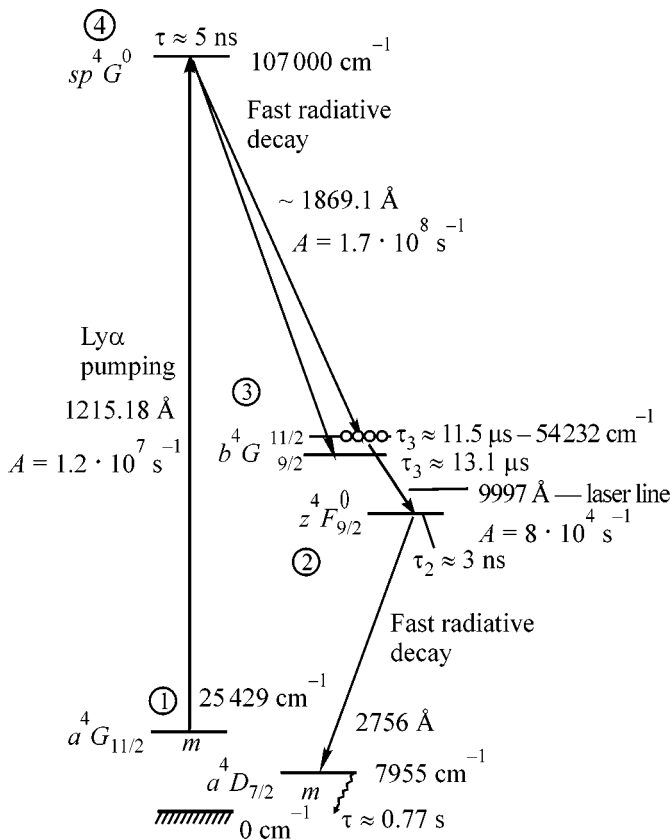


Fig. 1. Schematic diagram of the relevant energy levels and radiative transitions of Fe II illustrating the formation of an inverse population of levels 3 and 2 and amplification in the transition 3 → 2 owing to the photoselective pumping of level 4 by the intense Ly α radiation.

intensity, typical of an allowed transition. This is exactly what we have found to be the case with several spectral lines of Fe II pumped indirectly by the intense H Ly α radiation (1215 Å) in a dense-gas condensation (blob) in the vicinity of η Car.

Using the Space Telescope Imaging Spectrograph (STIS) onboard the Hubble Space Telescope, the authors of [8] recorded the spectra of blob B in the vicinity of η Car with a high angular and spectral resolution. The spectrum contains an intense 9997 Å line, as well as other Fe II lines at 9391, 9617, and 9913 Å, which can be excited by H Ly α radiation in a cascade fashion [9], shown schematically in Fig. 1. All these spectral lines have long-lived (from a few microseconds to a few milliseconds) upper states and a short-lived (3.7 ns) lower state; i.e., an inverted population always exists in these transitions. The gain by these inverted-population transitions is governed by the rate of photoexcitation of the upper levels by the H Ly α radiation.

Photoselective pumping of Fe II by H Ly α Radiation

Dense-gas condensations (Weigelt blobs [10]) in the neighborhood of the luminous blue variable (LBV) and massive star η Carinae are capable of absorbing all the photospheric radiation in the wide Lyman continuum region ($\lambda < \lambda_c = 912$ Å) incident upon them from the central star. This occurs because of the high Lyman-continuum optical density $\tau(\lambda_c)$ of the neutral hydrogen component in the ionized HII/HI region of the blob. Since the gas condensations are very close to the central star [11, 12], the density of the radiative energy deposited in them proves to be so high that the spectral brightness temperature $T_{br}(\text{Ly}\alpha)$ of the more narrow Ly α line at 1215 Å inside the blobs can be very high. The magnitude of $T_{br}(\text{Ly}\alpha)$ can become comparable with that of the brightness temperature of the photosphere of η Car, $T_s = (20\text{--}30) \times 10^3$ K. This is a unique situation for the photoselective excitation of those atoms and ions whose absorption lines from the ground state or low-lying metastable states coincide with Ly α .

This is exactly the situation that occurs for the Fe II ions formed in the HI region of the blob by complete photoionization of Fe I by the radiation from η Car in the spectral region $I_{Fe} = 7.6 \text{ eV} < h\nu < I_H = 13.6 \text{ eV}$. The concentration of iron in typical nebulae is about 0.01% of the hydrogen concentration. When Fe I undergoes photoionization, a substantial portion of the Fe II ions formed occupy low-lying long-lived metastable states with energies $E < I_H - I_{Fe} \approx 6 \text{ eV}$ as a result of the decay from numerous autoionization states. There are about 90 such metastable and pseudometastable states in Fe II. Some of them have absorption lines coinciding in wavelength with the extremely bright spectral line Ly α . The large number of low-lying long-lived states and the high density of spectral lines (≈ 15 lines/Å in the Ly α region) result in several such coincidences in Fe II. Several of them are similar to those shown schematically in Fig. 1, which lead to photoselective excitation of energy levels in Fe II, and the subsequent cascading decay gives rise to population inversion.

The Ly α line at $\lambda = 1215.671$ Å almost coincides with the absorption line of Fe II in the transition $a^4G_{11/2}$ (level 1 in Fig. 1) → sp^4G^0 (level 4), the frequency difference (detuning) between them being $\Delta\nu = +30 \text{ cm}^{-1}$. This difference is compensated by the broadening of the line profile when the Ly α radiation is passed through the HI region with an optical density of $\tau \approx 3 \times 10^5$. Thus, the transfer broadening of the Ly α radiation makes the photoselective excitation of state 4 in Fig. 1 quite possible.

The photoselective excitation rate of state 4 is defined by the expression

$$W_{\text{exc}}^{14} = A_{41} \left[\exp\left(\frac{h\nu_{14}}{T_{bl}}\right) - 1 \right]^{-1}, \quad (1)$$

density of the hydrogen atoms in the blob. According to the data presented in [11] and the results of a calculation of the critical density of hydrogen atoms [13], the density N_{H} of the hydrogen atoms in the blob is obviously higher than 10^8 cm^{-3} . Thus, for $\alpha_{32} \geq 3 \times 10^{-14} - 10^{-12} \text{ cm}^{-1}$ and a blob diameter $D \approx 10^{15} \text{ cm}^{-3}$ [11], which can be regarded as the size αL of the amplifying region (Fig. 2), $\alpha L \approx (30-1000)$ at a blob temperature of $T_{\text{bl}} = (12-18) \times 10^3 \text{ K}$.

These values correspond to fairly high linear amplification coefficients $K = \exp(\alpha L)$. However, at an amplification coefficient of $K \approx A_{41}/A_{32} \approx 10^3$ for an isotropic radiation, the intensity of the weak line λ_{32} (in photons/cm² s) approaches that of the strong line λ_{43} ; i.e., the rate of stimulated transition approaches the pumping rate for level 3. Thereafter, the amplification regime becomes saturated, and the intensity of the laser line λ_{32} becomes equal to that of the pumping line λ_{43} . Under such saturated amplification conditions, the intensities of both these lines grow in proportion to the propagation length L .

We believe that laser amplification and stimulated emission of radiation is a fairly common and widespread phenomenon, at least, for gas condensations in the vicinity of bright stars. This is due to the occurrence of two types of processes (fast radiative and slow collisional) in a very rarefied gas of the condensations, whereby the populations of electronic levels in atoms (ions) can relax. These relaxation processes occur on highly different time scales, radiative relaxation operating on a time scale of $10^{-9}-10^{-3}$ (sometimes even within 10^{-3}), and collisional relaxation, on a time scale of over 100 s (at gas densities $<10^9 \text{ cm}^{-3}$). In the case of photo-selective excitation of some high-lying levels of an atom or ion with a complex energy-level structure, radiative relaxation takes place as a consequence of downward transitions with spontaneous emission of radiation, in the course of which there inevitably develops an inverse population of some pair (pairs) of levels. If the size of a gas cloud is large enough, large amplification

of the inverted-population transition automatically switches on the radiative relaxation channel, which leads to faster stimulated quantum transitions until collisional relaxation becomes important. Thus, the laser action is an intrinsic characteristic of the radiative cooling of gas clouds near bright stars by stimulated emission for inverted transitions along with spontaneous emission for normal noninverted transitions.

REFERENCES

1. A. E. E. Rogers, J. M. Moran, P. P. Crowther, *et al.*, Phys. Rev. Lett. **17**, 450 (1966).
2. A. C. Cheung, D. M. Rank, C. H. Townes, *et al.*, Nature **22**, 626 (1969).
3. C. H. Townes, Quantum Electron. **24**, 1063 (1997).
4. V. Strelnitski, M. R. Haas, H. A. Smith, *et al.*, Science **272**, 1459 (1996).
5. A. L. Betz, R. A. McLaren, E. C. Sutton, and C. H. Townes, Astron. Soc. J. Lett. **208**, L145 (1976).
6. M. J. Mumma, D. Buhl, G. Chin, *et al.*, Science **212**, 45 (1981).
7. V. S. Letokhov, IEEE J. Quantum Electron. **QE-8**, 615 (1972); N. N. Lavrinovich and V. S. Letokhov, Zh. Éksp. Teor. Fiz. **67**, 1609 (1974) [Sov. Phys. JETP **40**, 800 (1975)].
8. T. Gull, K. Ishibashi, K. Davidson, and N. Collins, in *Eta Carinae and Other Mysterious Stars*, Ed. by T. Gull, S. Johansson, and K. Davidson; Astron. Soc. Pac. Conf. Ser. **242**, 391 (2001).
9. S. Johansson and C. Jordan, Mon. Not. R. Astron. Soc. **210**, 239 (1984).
10. G. Weigelt and J. Ebersberger, Astron. Astrophys. **163**, L5 (1986).
11. K. Davidson and R. M. Humphreys, Annu. Rev. Astron. Astrophys. **35**, 1 (1997).
12. F. Haman, K. Davidson, K. Ishibashi, *et al.*, in *Eta Carinae at the Millenium*, Ed. by J. A. Morse, R. M. Humphreys, and A. Damineli; Astron. Soc. Pac. Conf. Ser. **179**, 116 (1999).
13. S. Johansson and V. S. Letokhov, Astron. Astrophys. **378**, 262 (2001).

Oscillatory Radioactive Decay of Long-Lived Isomers with Intermediate Mössbauer Levels

S. K. Godovikov

Skobel'tsyn Research Institute of Nuclear Physics, Moscow State University,
Vorob'evy gory, Moscow, 119992 Russia

Received April 3, 2002

Oscillations were observed in the radioactive decay curves of the ^{119m}Sn and ^{125m}Te isomers. The phenomenological model based on a nonlinear decay equation is suggested for the phenomenon. © 2002 MAIK "Nauka/Interperiodica".

PACS numbers: 21.10.Tg; 23.20.Lv; 76.80.+y

In work [1], published in 1998, the conditions were established experimentally under which the radioactive decay constant λ may strongly change; e.g., $\Delta\lambda/\lambda = -(0.114 \pm 0.027)$ for the ^{119m}Sn isomer. The decay scheme for this isotope is shown in Fig. 1. The energy of its isomeric level is 89.53 keV, $T_{1/2} = 293$ days, and the energy of the intermediate Mössbauer level is 23.87 keV. The idea was to surround the isomeric nuclei with their decay products, i.e., with the stable ^{119}Sn isotopes. To do this, a screen made from "black" Mössbauer absorber (with a very broad absorption spectrum) containing many stable ^{119}Sn isotopes (up to 15 mg/cm²) was attached immediately to a source. It was assumed that the combined action of the recoilless Mössbauer radiation and the recoilless reemission from the stable nuclei could produce in local microregions long-lived ($\sim 10^{-8}$ s), on the nuclear time scale, standing-wave interference patterns with antinodes on the nuclei occurring in the predecay state. As a result, the nuclear parameters may change dramatically. It was predicted that, under these experimental conditions, the decay curve, in principle, may show oscillatory behavior [1–3].

These positions were elaborated in further studies. Namely, the next experiment [4] was arranged in such a way that the source was surrounded by the resonant screen on all sides; i.e., the 4π geometry was used. As a result, the effect was enhanced more than two times: $\Delta\lambda/\lambda = -(0.25 \pm 0.03)$. The idea also arose of surrounding the emitting nuclei by their decay products on the atomic level through mixing the stable and radioactive isotopes (internal screen). The result was even more impressive: $\Delta\lambda/\lambda = -(0.32 \pm 0.01)$ [4]. Finally, the studies were carried out with another isotope, ^{125m}Te . The decay scheme of this isomer, which is produced from the mother nucleus ^{125}Sb ($T_{1/2} = 2.7$ year), is shown in Fig. 1. The energy of isomeric level for this nucleus is 145.0 keV, $T_{1/2} = 58$ days, and the energy of

its intermediate Mössbauer level is 35.6 keV. The experimental scheme with internal screen was also used in this case. As a result, the portions of decay retardation, decay stop, "emission generation," and decay acceleration were observed in the decay curve [4, 5]. These pioneer results called for further inquiries in this direction. This work is devoted to the implementation of this idea.

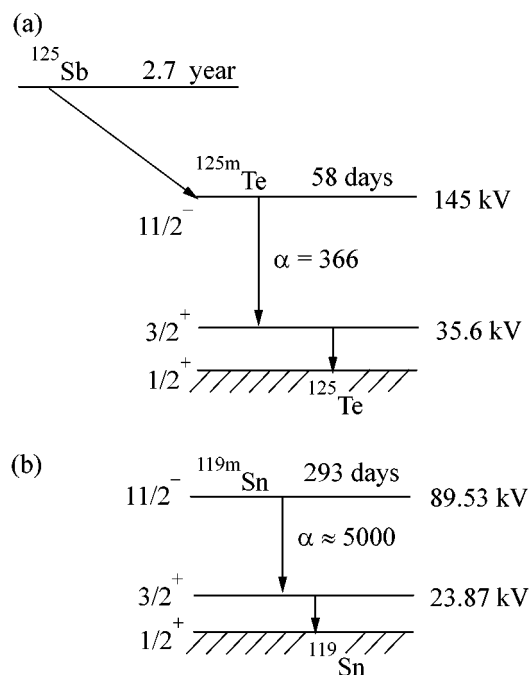


Fig. 1. Schemes of isotope decay for (a) $^{125}\text{Sb}(^{125m}\text{Te})$ and (b) ^{119m}Sn ; α is the conversion coefficient.

EXPERIMENTAL

To enhance the effects observed for the ^{119m}Sn isotope, long-term (~ 3 years) measurements were undertaken for the decay curve of a source supersaturated with an artificially introduced stable isotope. For this purpose, an object with an activity of 0.5 mCi was synthesized from the BaSnO_3 compound, in which 2×10^4 stable isotopes were introduced per one radioactive atom. This model corresponds to a source whose “age” is $\sim 14T_{1/2}$. The radiation was detected by the scintillation method using a 1-mm-thick NaJ(Tl) crystal. In this and other experiments, the emission was detected from the intermediate (Mössbauer) level, whose decay identically reflects the decay of the upper (isomeric) level. A multichannel analyzer with 256 channels operating in a multiscalar mode was used. The number J of counts in 1 s per channel was the measured parameter. The electronic parameters of the setup and the geometric arrangement of the source and detector were kept stable with a high accuracy for several years.

A similar experiment was carried out with the standard Mössbauer source $^{125}\text{Sb}(^{125m}\text{Te})$ in a Cu matrix. It was fabricated in 1991 and had an initial activity of 5.4 mCi. By the beginning of measurements, 14 stable ^{125}Te nuclei had been accumulated per one radioactive nucleus in the source; i.e., a rather active internal screen was formed inside the source. This object corresponded to a source passed through the stage of natural aging (contrary to the case described above). The secular equilibrium between ^{125m}Te and ^{125}Sb is achieved in the first year of the source lifetime, whereupon the ^{125m}Te production rate becomes equal to the decay rate of the mother nucleus (Fig. 1).

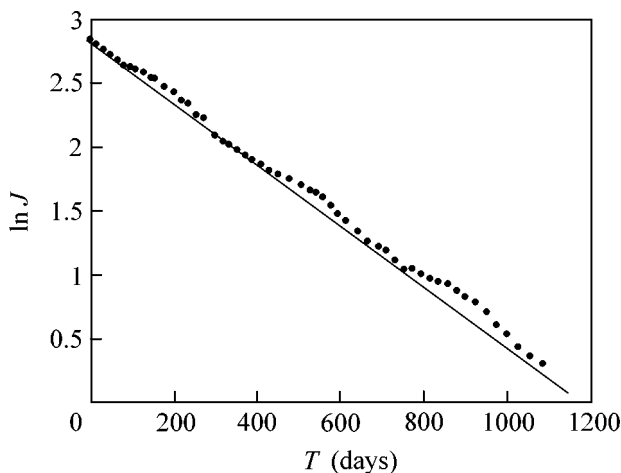


Fig. 2. Decay curve for a $\text{Ba } ^{119m}\text{SnO}_3$ source containing 2×10^4 stable ^{119}Sn nuclei per one radioactive nucleus (errors are given by the circle sizes). Solid line is the normal decay law ($T_{1/2} = 293$ days).

Finally, to perform reference measurements, a non-Mössbauer source in the form of an aqueous solution of $^{119m}\text{SnCl}_2$ was fabricated and placed in a special gamma-transparent ampule. The activity of this object was 0.5 mCi, and the experimental conditions were the same as described above.

All experiments were carried out at 293 K.

RESULTS

The results of the first experiment are presented in Fig. 2. Measurements started on March 12, 1999. The ordinate is $\ln J$, and the abscissa is time (in days). The solid line corresponds to the normal decay regime with $T_{1/2} = 293$ days. It is clear from Fig. 2 that the decay has the oscillatory character with a period of ~ 380 days. Three oscillation “waves” with amplitudes increasing with time are distinctly seen in the curve. The portions of decay retardation (e.g., $\Delta\lambda/\lambda = -0.34$ at $t > 750$ days), normal run, and decay acceleration (e.g., $\Delta\lambda/\lambda = 0.42$ at $t > 920$ days) are seen in the curve. Strictly speaking, the notion of decay constant loses its physical meaning in this case, because λ is a function of time. Thus, the presence of many self-decay products in the vicinity of the emitting nucleus gives rise to the oscillations in its decay curve. However, on the whole, the normal decay still dominates.

The results of measurements with a $^{125}\text{Sb}(^{125m}\text{Te})$ source are presented in Fig. 3. Measurements started on September 20, 2000. The oscillations with a varying period of several hundred days are also clearly seen in this case. The initial portion of the curve (the first 110 days), where the decay is accelerated by 2.36 times ($\Delta\lambda/\lambda = 1.36$), is particularly pronounced. Then, the

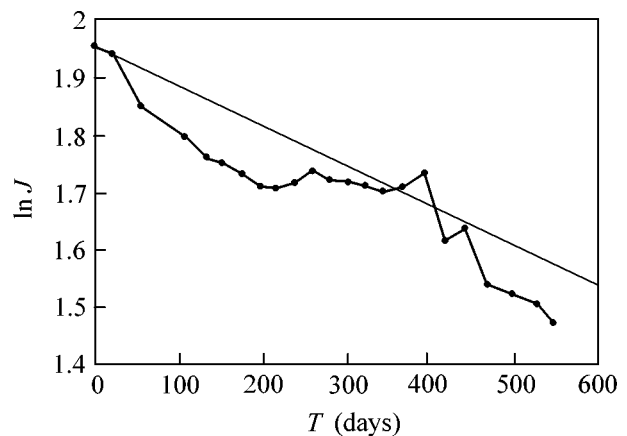


Fig. 3. Decay curve for the aged $^{125}\text{Sb}(^{125m}\text{Te})$ source in a Cu matrix (errors are given by the circle sizes). Solid line is the normal decay law ($T_{1/2} = 2.7$ year).

decay starts to slow down and stops ($dJ/dt = 0$) for the first time at $t = 216$ days, after which it gives way to emission generation ($dJ/dt > 0$), another stop ($t = 259$ days), and normal decay. This cycle is repeated again, though with a more pronounced generation peak. Nevertheless, the overall shape of the curve corresponds to the normal decay ($T_{1/2} = 2.7$ years).

The results obtained for a non-Mössbauer ^{119m}Sn source are presented in Fig. 4. The measurements started on July 20, 2001. One can clearly see that the radioactive decay shows the standard behavior and does not display any anomalies of the type described above. This provides strong evidence for the Mössbauer nature of decay oscillations.

DISCUSSION

It is clear that the results presented in this paper cannot be described by the traditional radioactive decay equation

$$dN/dt = -\lambda N, \quad (1)$$

where N is the number of radioactive nuclei at a given instant of time. A modified form of this equation [4, 5] is written as

$$dN/dt = -\lambda(N - AN^3), \quad (2)$$

where A is the proportionality coefficient. The physical meaning of the term $-AN^3$ consists in the fact that it is equal to the number of nuclei “leaving” the decay process or “retarding” because of an indefinitely large $T_{1/2}$. The mechanism of their production can be envisioned as follows. The emitting and absorbing nuclei form a system of standing Mössbauer waves, whose antinodes may fall on the isomeric nuclei that did not yet decay. The resulting “nucleus–wave” system has two excited energy levels, with the energy of one of them being a multiple of the other ($145/35.6 = 4$ for ^{125m}Te). Under these conditions, dynamic oscillation synchronization may occur [6]; i.e., the occupied lower level may influence the parameters of the upper level. In other words, the decay of the upper level is hampered because the lower level is occupied for a time. As a result, the “retarded” nuclei appear. Assume that the number of emitting nuclei in volume unit at time t is equal to λN . The probability of a standing wave being formed as a product of pair interaction is proportional to the squared concentration of interacting components; i.e., this probability is proportional to $\sim(\lambda N)^2$. It is assumed that, for each emitting nucleus, there is a scattering nucleus, which is the case in the experiments considered. The number of retarded nuclei is equal to the product of the probability of forming the standing wave system by the number of radioactive nuclei; i.e., it is proportional to $\sim(\lambda N)^2 N$ or equal to AN^3 . The analytic solution to Eq. (2) is given in [5]. It leads to a power retardation law, which transforms to the traditional exponential form at long times. A remarkable feature of

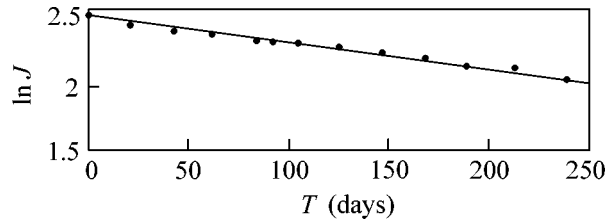


Fig. 4. Decay curve for a $^{119m}\text{SnCl}_2$ source in an aqueous solution (errors are given by the circle sizes). Solid line is the normal decay law ($T_{1/2} = 293$ days).

Eq. (2) is that it accounts for the oscillatory decay. Indeed, $dN/dt = 0$ at $N = \pm\sqrt{1/A}$. The solution with a minus sign implies that Eq. (2) may take the form

$$dN/dt = +\lambda(N - AN^3), \quad (3)$$

allowing the emission generation or the decay bifurcation.

The question now arises as to the origin of emission generation (“autocatalysis”) provided by Eq. (3). There can be only one reason for this process: upon reaching a certain threshold concentration, the retarded nuclei undergo rapid transition to the normal state, which is accompanied by the “burst” of gamma radiation as a result of collective energy accumulation.

Equations (2) and (3) can conveniently be analyzed on the phase plane “rate (dN/dt)–coordinate (N).” For definiteness, let us consider the experiment with ^{125m}Te (Fig. 3). The source in this experiment contained initially (in 2001) $N_0 = 0.177 \times 10^{16}$ nuclei, and $A = 3.19 \times 10^{-31}$. The constant λ for ^{125}Sb is 70.3×10^{-5} 1/day. The extremes in the curves given by Eqs. (2) and (3) occur at

$$dN/dt = \lambda \times 2/3 \sqrt{\frac{1}{3A}}. \quad (4)$$

These initial data were used to construct dN/dt as a function of N for Eq. (2) (Fig. 5, curve *a*). The time in this figure is a parameter, and it increases, according to the conventional rules adopted for the differential equations of this class, when moving from right to left (shown by arrow) [7]. Assume, for definiteness, that the number of retarded nuclei comprises, e.g., 1/3 of the normal nuclei. This increases the parameter A to 2.78×10^{-30} , which is 8.7 times greater than for the normal nuclei. Curve *b* in Fig. 5 corresponds to Eq. (3). Naturally, $N_0 = 0$ for this curve, because no generation occurs at $t = 0$. For curve *b*, the time increases when moving from left to right.

Evidently, all the observed results can be explained by combining curves *a* and *b* in Fig. 5. Indeed, if time is counted from the extreme points on the N axis, then the result will be the sum of curves *a* and *b*. To obtain the dependence of dN/dt on t , one has to correctly add together curves *a* and *b* for each moment t . The neces-

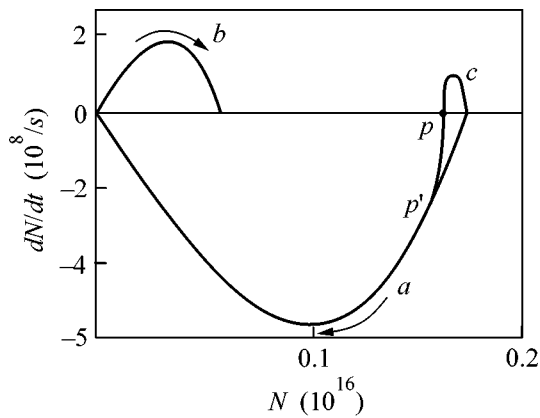


Fig. 5. Graphic representation of Eqs. (2) and (3) on the phase plane “rate–coordinate” ($dN/dt-N$). Curve *a* corresponds to Eq. (2), curve *b* corresponds to Eq. (3), and curve *c* corresponds to the combined representation of Eqs. (2) and (3).

sity of the correct combination of these curves is dictated by the fact that curve *b* is “swept” too fast, because the emission generation, the decay slowing down, and the subsequent acceleration occur in ~ 100 days (Fig. 3), which is ~ 10 times faster than the mean trend in the normal decay ($T_{1/2} = 2.7$ year = 985 days). An example of such an addition is presented in Fig. 5 (curve *c*). One can see that the resulting curve, starting at $dN/dt = 0$, immediately falls into the generation regime ($dN/dt > 0$), which gradually slows down to reach the point *p*, where $dN/dt = 0$, after which the decay is accelerated (the curve becomes steeper than AN^3) up to the point *p'*, where the outburst in the curve is terminated. However, this does not mean that the radiation burst occurs only once. The retarded nuclei are again accumulated as a result of the burst and, together with a portion of “untapped” nuclei, can generate a new burst after a time, as is seen in Fig. 3.

The features of Fig. 5 can generally be used for interpreting the behavior of the decay curve for ^{119m}Sn

(Fig. 2). The distinctions are that the curve of type *b* in Fig. 5 is poorly pronounced, and the decay of type *a* starts on the left of the point *p'*, so that the overall curve never attains the level $dN/dt = 0$. The oscillations (“ripple”) are only observed on the normal decay curve. This is likely due to the fact that the energy of isomeric level in ^{119}Sn is not a strict multiple of its Mössbauer energy ($89.53/23.87 = 3.75$), so that the dynamic oscillation synchronization is less efficient in this system.

Note in conclusion that the decay control for the class of isomers considered in this work, in principle, may be brought to the “catastrophic” level, i.e., to the instantaneous depletion of the isomeric level. To do this, it is necessary to create, in one way or another, a high concentration of retarded nuclei at least in two identical sources and then bring them into contact at the proper instant of time. Undoubtedly, the expected burst will have the collective (and, possibly, coherent) character of the superradiance regime. This opens up a wide field for the physical and technological applications of the phenomenon observed in this work.

This work was supported by a grant from the Research Institute of Nuclear Physics.

REFERENCES

1. S. K. Godovikov, Pis'ma Zh. Éksp. Teor. Fiz. **68**, 599 (1998) [JETP Lett. **68**, 629 (1998)].
2. S. K. Godovikov, Laser Phys. **8**, 1100 (1998).
3. S. K. Godovikov, Izv. Akad. Nauk, Ser. Fiz. **63**, 1397 (1999).
4. S. K. Godovikov, Laser Phys. **10**, 1293 (2000).
5. S. K. Godovikov, Izv. Akad. Nauk, Ser. Fiz. **65**, 1063 (2001).
6. I. I. Blekhman, *Synchronization in Science and Technology* (Nauka, Moscow, 1981; ASME Press, New York, 1988).
7. W. J. Cunningham, *Introduction to Nonlinear Analysis* (McGraw-Hill, New York, 1958; Gosénergoizdat, Moscow, 1962).

Translated by V. Sakun

Entangled State Generation and Modulation of Vacuum Squeezing by Classical Optical Fields in Birefringent Fiber¹

S. A. Podoshvedov

Department of Physics, Inha University, Incheon, 402-751 South Korea

e-mail: podoshvedov@mail.ru

Received April 15, 2002

Evolution of the vacuum fluctuations in the two-wave mixing of the optical fields propagating in a birefringent fiber is studied. The two-wave mixing in the birefringent fiber was suggested as a possible scheme for the entangled-state generation. Our treatment in studying the entangled-state generation uses depleted pump approximation and enables one to trace the influence of the input conditions of classical optical fields on the evolution of vacuum squeezing. We report the periodical modulation of the vacuum squeezing when the input relative phase of coherent waves varies. The measure of nonclassical correlations imposed on the generated light is calculated. © 2002 MAIK “Nauka/Interperiodica”.

PACS numbers: 42.50.Dv; 42.65.Hw; 03.65.Ud

Entanglement shared among many particles plays an important role in various schemes of quantum information processing, such as tests for Bell's inequalities and the Einstein–Podolsky–Rosen “paradox” [1], quantum teleportation [2], quantum computing [3], and quantum cryptography [4]. Spontaneous parametric down-conversion (SPDC)—a nonlinear optical process in which a pump is converted into a pair of photons, called signal and idler—is considered as the main source of strongly correlated photons [5]. Nevertheless, we guess other parametric processes may be studied for the correlated photons to be generated. In this paper, we study the properties of a nonclassical light generated in the parametric two-wave mixing of optical fields, which propagate through the single-mode birefringent fiber, using linearization treatment [6, 7]. The given treatment enables one to allow for the influence of the input conditions of the classical optical fields and the parameters of the medium on the properties of the generated state. We show that vacuum squeezing undergoes periodic modulation with a change in the input relative phase of the coherent optical fields.

In order to describe quantum noise in an optical medium, it is necessary to introduce a suitable Hamiltonian comprising quantum operators. We choose the model of two continuous waves (cws) propagating in the single-mode birefringent fiber described by the nonlinear susceptibility $\chi^{(3)}$, which is invariant over a

finite frequency range. This Hamiltonian is given by

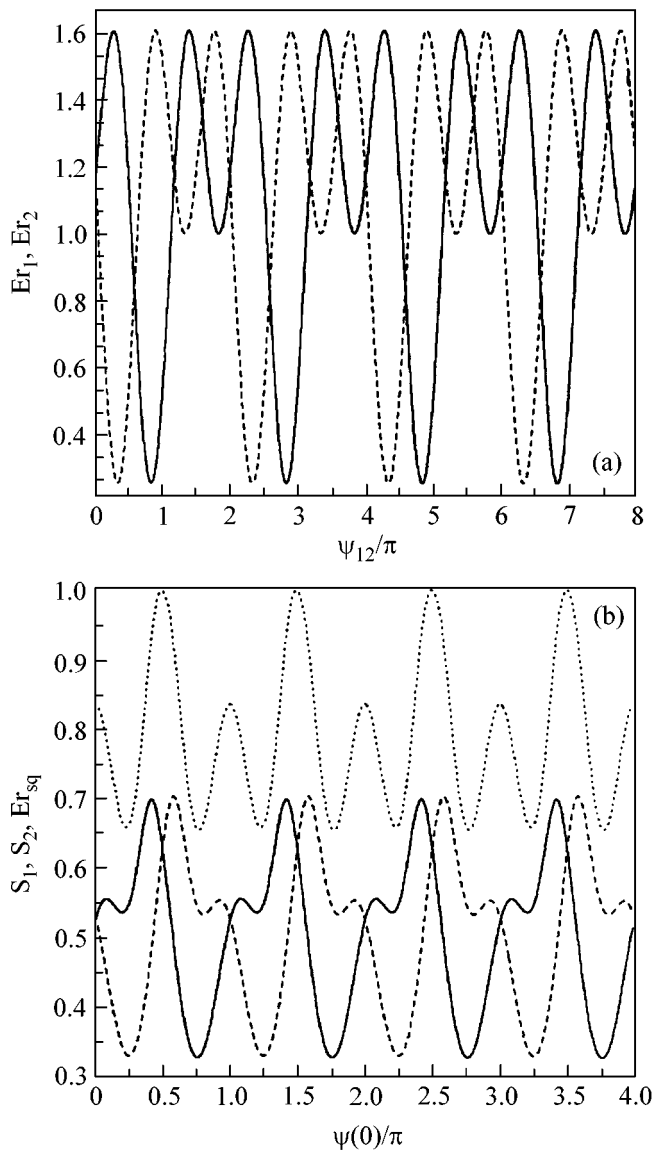
$$H = c\hbar \left(\frac{R}{6} (\hat{A}_1^{+2} \hat{A}_2^2 + \hat{A}_2^{+2} \hat{A}_1^2) + \frac{R}{2} (\hat{A}_1^{+2} \hat{A}_1^2 + \hat{A}_2^{+2} \hat{A}_2^2) + \frac{2R}{3} \hat{A}_1^+ \hat{A}_2^+ \hat{A}_1 \hat{A}_2 \right) + \Delta k \hat{A}_2^+ \hat{A}_2, \quad (1)$$

where \hat{A}_1 , \hat{A}_2 , \hat{A}_1^+ , and \hat{A}_2^+ are the annihilation and creation field operators orthogonally polarized along the x and y directions of the fiber and obeying well-known harmonic-oscillator commutation relations $\{\hat{A}_i; \hat{A}_j^+\} = \delta_{ij}$, $\{\hat{A}_i; \hat{A}_j\} = 0$, $\{\hat{A}_i^+; \hat{A}_j^+\} = 0$ ($i, j = 1, 2$). Coefficient $R = n_2 \hbar \omega^2 / c^2 V 2 \epsilon_0 A_{\text{eff}}$ is the nonlinear coupling constant which characterizes the strength of nonlinear interaction in the fiber, $\omega = 2\pi c / \lambda$, λ is the wavelength of the interacting fields, $n_2 = 3.2 \times 10^{-16} \text{ cm}^2/\text{W}$ is the nonlinear refraction index of the fiber, $\epsilon_0 = 8.85 \times 10^{-12} \text{ F/m}$ is the electrical constant, V is the volume of the quantized modes, $A_{\text{eff}} \equiv \pi r_c^2$ is the effective area of the single-mode fiber [8], r_c is the radius of the core, and $\Delta k = k_y - k_x$ is the wave mismatch between the wave vectors. The nonlinear operator equations are derived from

Heisenberg equation $i\hbar \frac{d\hat{A}_i}{dt} = \{\hat{A}_i; H\}$ and given by

$$\begin{aligned} \frac{d\hat{A}_1}{dz} &= iR \left(\frac{1}{3} \hat{A}_1^+ \hat{A}_2^2 + \left(\hat{A}_1^+ \hat{A}_1 + \frac{2}{3} \hat{A}_2^+ \hat{A}_2 \right) \hat{A}_2 \right), \\ \frac{d\hat{A}_2}{dz} &= iR \left(\frac{1}{3} \hat{A}_2^+ \hat{A}_1^2 + \left(\frac{2}{3} \hat{A}_1^+ \hat{A}_1 + \hat{A}_2^+ \hat{A}_2 \right) \hat{A}_2 \right) + \Delta k \hat{A}_2. \end{aligned} \quad (2)$$

¹ This article was submitted by the author in English.



Dependence of the quantities Er_1 , Er_2 on the relative normalized phase ψ_{12}/π related to the phase of the second local oscillator (a) and vacuum squeezing S_1 , S_2 and corresponding degree of the correlation Er_{sq} of the quantities S_1 and S_2 (b) on the input normalized difference of the phases $\psi(0)/\pi$. The quantities Er_1 and Er_2 are shown by solid and dashed curves in (a), and S_1 , S_2 , and Er_{sq} are shown by solid, dashed, and dotted curves, respectively, in (b). The plots are made under the following conditions $r_c = 1.5 \mu\text{m}$, $\lambda = 1.55 \mu\text{m}$, $L = 300 \text{ m}$, $k = -0.1$, $P = 0.2 \text{ W}$.

It is not clear outright whether the operator Eqs. (2) can be solved in terms of some analytic functions. This question is coming up for discussion, because the classical equations analogous to the quantum Eqs. (2) are solved in [9]. For this reason, one should use approximate methods in analyzing the nonlinear operator equa-

tions. We use linearization treatment [6, 7] to study the evolution of quantum fluctuations in the birefringent fiber. We consider the vacuum fluctuations as small perturbations, as compared with the mean values of fields [6, 7]. The reason to consider the quantum operators is simple. A stabilized laser, for example, an He-Ne laser, is known to emit almost coherent light with properties very similar to the properties of a classical field with quantum zero-point fluctuations (vacuum noise) superposed. This enables one to decompose the quantum operators into two parts as $\hat{A}_1 = \langle \hat{A}_1 \rangle + \hat{a}_1$, $\hat{A}_2 = \langle \hat{A}_2 \rangle + \hat{a}_2$, [6, 7], where $\langle \hat{A}_1 \rangle$, $\langle \hat{A}_2 \rangle$ are the expected values of the operators, which can be obtained by averaging the operators on the initial coherent states. The operators \hat{a}_1 and \hat{a}_2 describe the evolution of vacuum quantum noises in the birefringent fiber. Nonlinear equations for the expectation values of quantum operators are derived in zero order with respect to vacuum operators if we make use of assumption conditions $\langle \hat{A}_i^+ \hat{A}_j \hat{A}_k \rangle = \langle \hat{A}_i^+ \rangle \langle \hat{A}_j \rangle \langle \hat{A}_k \rangle$ ($i, j = 1, 2$) to be carried out. As a matter of fact, this means that we use classical waves of pump. The equations in zero order in operator \hat{a}_i ($i = 1, 2$) are given in terms of quantities η and ψ by [7],

$$\begin{aligned} \frac{d\eta}{ds} &= \tau \frac{2}{3} \eta (1 - \eta) \sin(2\psi), \\ \frac{d\psi}{ds} &= \tau \left(\frac{1}{3} (1 - 2\eta) \cos(2\psi) + \frac{2}{3} \eta - \frac{1}{3} + \frac{k}{2} \right), \end{aligned} \quad (3)$$

where $\eta = |q_2|^2 = |E_2|^2/P$, $|q_1|^2 = 1 - \eta = |E_1|^2/P$, $\psi = \phi_2 - \phi_1$ is the difference in the phases of the normalized field amplitudes $q_1 = |q_1| \exp(i\phi_1)$ and $q_2 = |q_2| \exp(i\phi_2)$, $P \sim N$ is the conserved power, the quantity $N = |\langle \hat{A}_1 \rangle|^2 + |\langle \hat{A}_2 \rangle|^2$ is the total number of photons in the interacting fields, the quantity $\tau = L/L_{nl} = LPn_2\omega/cA_{\text{eff}}$ is the ratio of the full fiber length to the interaction one, $s = z/L$ is the dimensionless longitudinal length (s is changed from 0 up to 1), and $k = 2\Delta kL$ is the dimensionless mismatch. The quantities E_1 and E_2 are the field amplitude moduli square of which is measured in units of W/cm^2 . Equations (3) are the integrable Hamiltonian ones [9]. Equations for vacuum field operators are produced when only linear terms on \hat{a}_1 , \hat{a}_2 are kept and the conditions $\langle \hat{A}_i^+ \hat{A}_i \rangle = \langle \hat{A}_i^+ \rangle \langle \hat{A}_i \rangle$, $\langle \hat{A}_i \hat{A}_i \rangle = \langle \hat{A}_i \rangle \langle \hat{A}_i \rangle$, are effected. We present equations in the matrix form for the vector column of the small operators $\mathbf{a} = (\hat{a}_1, \hat{a}_1^+, \hat{a}_2, \hat{a}_2^+)^T$ as $d\mathbf{a}/ds = i\tau G^a \mathbf{a}$, where $G^a(s)$ is the evolution matrix for the input column $\mathbf{a}(0)$ to be transformed to

$\mathbf{a}(s)$. Solution of the matrix equation $\mathbf{a}(s) = C^a(0)$ defines coefficients of the generated entangled state, which can be expressed in the general case with the help of density operator ρ . In the particular case where $C_{14}^a = C_{32}^a = C^a$, which is fulfilled under some input conditions, the pure two-particle entangled state can be written as $|\psi\rangle = C_{12}^a/\sqrt{2}|2_1\rangle|0_2\rangle + C_{34}^a/\sqrt{2}|2_2\rangle|0_1\rangle + C^a|1_1\rangle|1_2\rangle$, where $|C_{12}^a|^2/2 + |C_{34}^a|^2/2 + |C^a|^2 = 1$. The generated state is determined by the coefficients of matrix C^a and because it depends on the input conditions of the strong classical optical fields. Because we are interested in studying quadrature operators, we introduce transformation matrix $T^{Xa} = T^{aX^{-1}}$ of passage of the column \mathbf{a} to the quadrature operator column $\mathbf{X} = (\hat{X}_1, \hat{Y}_1, \hat{X}_2, \hat{Y}_2)^T$ ($\mathbf{X} = T^{(aX)^{-1}}\mathbf{a}$) as

$$T^{(aX)^{-1}} = \frac{1}{2} \quad (4)$$

$$\times \begin{vmatrix} \exp(-i\phi_1) & \exp(i\phi_1) & 0 & 0 \\ -i\exp(-i\phi_1) & i\exp(i\phi_1) & 0 & 0 \\ 0 & 0 & \exp(-i\phi_2) & \exp(i\phi_2) \\ 0 & 0 & -i\exp(-i\phi_2) & i\exp(i\phi_2) \end{vmatrix},$$

where the symbol T^{-1} means a matrix reverse to the matrix T . Introduction of the vector \mathbf{X} is useful since it enables one to get equations for \hat{X} in such a way that the new equations comprise only quantities η and ψ incurring Eqs. (4) [6]. To show it, we make use of the transformation matrix (4) and find the equation for \mathbf{X} [6],

$$d\mathbf{X}/ds = \tau G^X \mathbf{X}, \quad (5)$$

where

$$G^X = \begin{vmatrix} -\frac{1}{3}\eta \sin(2\psi) & \frac{2}{3}\eta \cos(2\psi) & -\frac{2}{3}\sqrt{\eta(1-\eta)} \sin(2\psi) & -\frac{2}{3}\sqrt{\eta(1-\eta)} \cos(2\psi) \\ 2(1-\eta) & \frac{1}{3}\eta \sin(2\psi) & \frac{2}{3}\sqrt{\eta(1-\eta)}(2 + \cos(2\psi)) & -\frac{2}{3}\sqrt{\eta(1-\eta)} \sin(2\psi) \\ \frac{2}{3}\sqrt{\eta(1-\eta)} \sin 2\psi & -\frac{2}{3}\sqrt{\eta(1-\eta)} \cos(2\psi) & \frac{1}{3}(1-\eta) \sin(2\psi) & \frac{2}{3}(1-\eta) \cos(2\psi) \\ \frac{2}{3}\sqrt{\eta(1-\eta)}(2 + \cos(2\psi)) & \frac{2}{3}\sqrt{\eta(1-\eta)} \sin(2\psi) & 2\eta & -\frac{1}{3}(1-\eta) \sin(2\psi) \end{vmatrix}.$$

Components of the quadrature operator vector $\mathbf{X}_i(s)$ are found according to $\mathbf{X}_i(s) = C_{ij}^X(s) \mathbf{X}_j(0)$ [6]. Expressions for squeezing (S_1, S_2) in the generated fields are produced in [6] in terms of the matrix elements $C_{ij}^X(s)$, which are the solutions to the equation $dC_{ij}^X/ds = \tau G_{ik}^X C_{kj}^X$ satisfying the input condition $C_{ij}^X(0) = \delta_{ij}$. As the generated state is the entangled state, we may infer quadrature-phase information about one of the interacting optical fields only by measuring the quadrature component of another optical field. To evaluate error in our inferring value of the nonmeasured quadrature component, knowing information only about the quadrature component of another field, we introduce quantities $Er_i = V_i(s)/V_i(0)$ ($i = 1, 2$), where $V_1 \langle (\hat{X}_{l1} - \hat{X}_{l2})^2 \rangle$, $V_2 \langle (\hat{X}_{l1} - \hat{Y}_{l2})^2 \rangle$, subscript l is related to the phase of the local oscillator, and the sign $\langle \rangle$ implies averaging of the quantum operators over the vacuum state. Using the results of [6], one can produce

expressions for Er_1 and Er_2 in terms of the matrix elements C_{ij}^X :

$$\begin{aligned} Er_1(\psi_{l1}, \psi_{l2}) = & \frac{1}{2} \left(\cos^2 \psi_{l1} \sum_{i=1}^4 C_{1i}^{X2} + \sin^2 \psi_{l1} \sum_{i=1}^4 C_{2i}^{X2} \right. \\ & + \sin(2\psi_{l1}) \sum_{i=1}^4 C_{1i}^X C_{2i}^X + \cos^2 \psi_{l2} \sum_{i=1}^4 C_{3i}^{X2} \\ & \left. + \sin^2 \psi_{l2} \sum_{i=1}^4 C_{4i}^{X2} + \sin(2\psi_{l2}) \sum_{i=1}^4 C_{3i}^X C_{4i}^X \right) \quad (6) \\ - & \left(\cos \psi_{l1} \cos \psi_{l2} \sum_{i=1}^4 C_{1i}^X C_{3i}^X + \sin \psi_{l1} \sin \psi_{l2} \sum_{i=1}^4 C_{2i}^X C_{4i}^X \right. \\ & \left. + \sin \psi_{l2} \cos \psi_{l1} \sum_{i=1}^4 C_{1i}^X C_{4i}^X + \sin \psi_{l1} \cos \psi_{l2} \sum_{i=1}^4 C_{2i}^X C_{3i}^X \right), \end{aligned}$$

where $\psi_{11} = \varphi_{11} - \varphi_1(L)$ and $\psi_{12} = \varphi_{12} - \varphi_2(L)$ are the relative phases, and φ_{11} and φ_{12} are the phases of the local oscillators for the first and second optical fields, respectively. Measurement of the odd-order moments imparts phase information on the components \mathbf{X}_i and, because it requires homodyning of the studied field with the reference field, is known as the local oscillator with the local phase φ_i ($i = 1, 2$). Other quantity $Er_2(\varphi_{11}, \varphi_{12})$ stems from $Er_1(\varphi_{11}, \varphi_{12})$ according to $Er_2(\varphi_{11}, \varphi_{12}) = Er_1(\varphi_{11}, \varphi_{12} + \pi/2)$. The less the quantities Er_1, Er_2 take their values, the more correlated photons are generated, and, on the contrary, if the quantities Er_1, Er_2 become more of 1, one may speak about the generation of the noncorrelated photons. The quantities Er_1 and Er_2 depend on the relative phases $\varphi_{11}, \varphi_{12}$ and input parameters of the coherent optical fields, for example, on $\psi(0)$, through the elements of C_{ij}^X . The dependence may be manifested in the periodical dependence of the quantities Er_1 and Er_2 on the input varied conditions. We performed calculations to check our idea and the results are depicted in Fig. 1. So, Fig. 1a shows the dependence of Er_1 and Er_2 on φ_{12}/π provided that φ_{11} is chosen in such a way that the vacuum squeezing S_1 was by this time observed. The variance of the other field varies with change of the local phase φ_{12} . Figure 1b shows the dependence of the squeezing in the first S_1 and second S_2 optical fields, respectively, and their joint correlation function Er_{sq} on the input relative $\psi(0)$ phase of the classical waves. As can be seen from Fig. 1b, squeezing (S_1, S_2) and correlation function Er_{sq} undergo periodical modulation with a change of the input relative phase $\psi(0)$.

In conclusion, we have shown that the entangled state of light is generated in the two-wave mixing of

optical fields propagating through the single-mode birefringent fiber from the vacuum initially not containing correlations. We have found the degree of correlation of the photons generated in the birefringent fiber and discovered the possibility of modulation of the vacuum squeezing by a change of the input relative phase of the coherent waves.

REFERENCES

1. Y. H. Shih and C. O. Alley, Phys. Rev. Lett. **61**, 2921 (1988); J. G. Rarity and P. R. Tapster, Phys. Rev. Lett. **64**, 2495 (1990).
2. C. H. Bennet, G. Brassard, C. Crepeau, *et al.*, Phys. Rev. Lett. **70**, 1895 (1993).
3. A. Barenco, D. Deutsch, A. Ekert, and R. Jorsa, Phys. Rev. Lett. **74**, 4083 (1995).
4. A. K. Ekert, Phys. Rev. Lett. **67**, 661 (1990); A. K. Ekert, J. G. Rarity, P. R. Tapster, and G. M. Palma, Phys. Rev. Lett. **69**, 1293 (1992).
5. D. N. Klyshko, *Photons and Nonlinear Optics* (Gordon and Breach, New York, 1988); M. H. Rubin, D. N. Klyshko, Y. H. Shih, and A. V. Sergienko, Phys. Rev. A **50**, 5122 (1994).
6. S. A. Podoshvedov, Pis'ma Zh. Éksp. Teor. Fiz. **67**, 881 (1998) [JETP Lett. **67**, 927 (1998)]; S. A. Podoshvedov, J. Noh, and K. Kim, unpublished.
7. R. D. Li and P. Kumar, Opt. Lett. **18**, 1961 (1993); Z. Y. Ou, Phys. Rev. A **49**, 2106 (1994); R. D. Li and P. Kumar, Phys. Rev. A **49**, 2157 (1994).
8. G. P. Agrawal, *Nonlinear Fiber Optics* (Academic, San Diego, 1995).
9. M. Romagnoli, S. Trillo, and S. Wabnitz, Opt. Quantum Electron. **24**, 1237 (1992); S. A. Podoshvedov, Opt. Commun. **142**, 79 (1997); **189**, 365 (2001); **199**, 245 (2001).

Stimulated Multiphoton Emission from Exciton Bose Condensate

Yu. E. Lozovik* and I. V. Ovchinnikov

Institute of Spectroscopy, Russian Academy of Sciences, Troitsk, Moscow region, 142190 Russia

* e-mail: lozovik@isan.troitsk.ru

Received April 8, 2002

The coherent recombination of several (N) Bose-condensed excitons with simultaneous creation of N photons is considered. Due to the momentum conservation law, the total momentum of created photons is zero because of the zero momentum of excitons in Bose condensate. This requirement, in conjunction with the fact that the photon wavenumbers are fixed and equal to approximately E_g/c (E_g is the semiconductor gap and c is the speed of light), determines the mutual orientation of the wavevectors of emitted photons. This can be seen from the photon angular correlation in the experiments with several appropriately oriented detectors operating in the time-coincidence mode. It is shown that, if these processes are induced by $N-1$ external laser beams (each with wavevector \mathbf{k}_i), then a unidirectional radiation with recoil wavevector $\mathbf{k} = -\sum_i \mathbf{k}_i$ should emerge from the exciton system. The intensities of coherent three- and four-exciton recombination are estimated for the exciton system in Cu_2O . © 2002 MAIK “Nauka/Interperiodica”.

PACS numbers: 71.35.Lk; 78.45.+h; 42.65.-k

Recent discovery of atomic Bose condensation has become one of the most spectacular developments in many-body physics [1]. Since the theoretically estimated temperature of exciton Bose condensation is eight orders higher than the presently achieved atomic Bose-condensation temperature, the studies of the corresponding effects in exciton systems can open no less intriguing prospects [2–10]. This notably applies to two-dimensional indirect exciton systems in coupled quantum wells exhibiting interesting properties in the coherent phase [5]. The studies of coherent exciton phase have culminated in a number of encouraging experimental results [6–8, 11]. Experimental research in this field can result in the engineering of exciton Bose condensate and the development of coherent exciton optics [12]. At the same time, the situation with the discovery of a three-dimensional coherent excitonic phase in Cu_2O , which is a promising material for the observation of Bose condensation [4, 10], still remains to be clarified [13]. For this reason, a search for the new qualitative effects that can unambiguously prove the occurrence of exciton Bose condensation, as well as a search for the corresponding properties of the system, are quite topical. This motivated us to consider new effects that are associated with the optical manifestation of many-exciton coherence in the Bose-condensed excitonic phase. Interest in the optical manifestations of excitonic coherence is caused by the fact that excitons are metastable particles and capable of recombining with photon emission.

We consider the coherent N -exciton recombination, i.e., the processes where N excitons in the condensate recombine simultaneously and coherently to create N photons correlated in exit angles. Besides, it turned out that these processes underlie a new nonlinear optical effect, namely, laser-stimulated N -exciton recombination.

The momentum of condensed excitons is zero, and their energy is equal to the chemical potential of the exciton system. Because of the momentum and energy conservation laws, the momenta and frequencies of photons created in the elementary many-exciton recombination event must satisfy the following equalities:

$$\sum_{i=1}^N \mathbf{k}_i = 0, \quad \sum_{i=1}^N ck_i = N\mu, \quad (1)$$

where μ is the chemical potential of the exciton system.¹ In the general case, these conditions do not deter-

¹ The exciton chemical potential measured from the top of the valence band can be written as $\mu = E_g - E_{ex} + \tilde{\mu}$, where E_g is the semiconductor gap, E_{ex} is the free-exciton binding energy, and $\tilde{\mu}$ is the exciton chemical potential calculated under the assumption that the exciton is a metastable particle with zero rest energy. Since $\tilde{\mu}, E_{ex} \ll E_g$, one has $\mu \approx E_g$. To shorten the notation in formulas, the photon energy is measured from the chemical potential μ , so that the photon dispersion is given by the expression $\omega_{\mathbf{k}} = ck - \mu \equiv c(k - k_0)$, where c is the speed of light in the medium and k_0 is the wavenumber of a photon with energy μ ($\hbar = 1$). This energy reading determines both photon and exciton energies, so that the condensate excitons have zero energy.

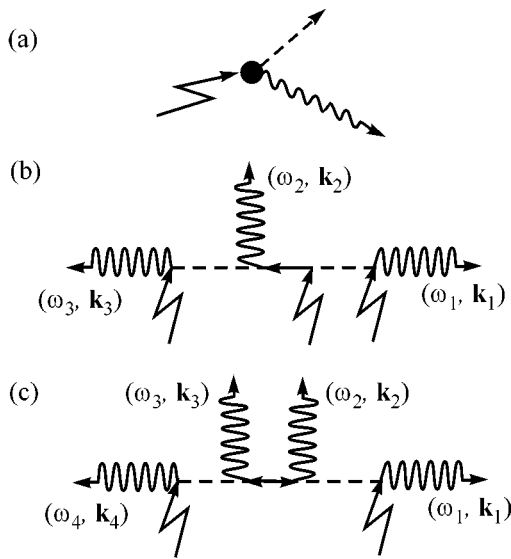


Fig. 1. Matrix elements for (a) one-exciton, (b) three-exciton, and (c) four-exciton recombinations. Broken lines are for the condensate excitons, wavy lines are for photons, dashed lines are for optical phonons, and solid lines with one or two arrows are, respectively, for the normal and anomalous exciton Greens function.

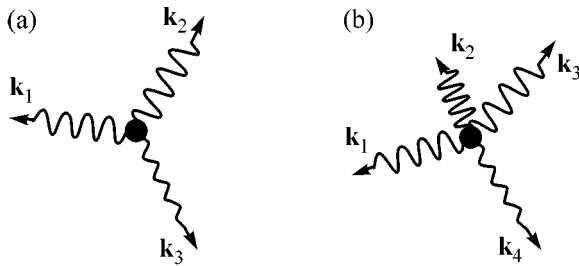


Fig. 2. Schematic representation of the possible experiments on detecting the stimulated (a) three- and (b) four-exciton recombinations. Heavy wavy lines correspond to the inducing laser beams and thin wavy lines correspond to the unidirectional radiation with recoil momentum (2) from the Bose condensate.

mine the relative angular photon directivity. However, an analysis of the probability of these processes shows (see below) that the photon exit angles are correlated, which can be observed experimentally.

The N -exciton recombination process is of higher order in many-body interaction than the one-exciton recombination (Fig. 1). For this reason, its rate W_N must be considerably lower than the one-exciton recombination rate (W_1). However, the matrix element of N -exciton recombination contains N incoming condensate lines, each introducing a large Bose factor $N_0^{1/2}$ (N_0 is the number of condensate excitons), whereas only one

such factor appears in the case of one-exciton recombination from the condensate. Accordingly, the one-exciton recombination process is first order in the density $\rho_{\text{cond}} = N_0/V$ of condensed excitons (V is the volume of the system), i.e., $W_1 \sim \rho_{\text{cond}}$, whereas the N -exciton recombination is the N th-order process, i.e., $W_N \sim \rho_{\text{cond}}^N$. At a high condensate density ρ_{cond} , the weakness introduced to the N -exciton diagrams by the additional (compared to one-exciton recombination) interparticle vertices is compensated, to some extent, by the additional factors ρ_{cond} . Thus, the spontaneous one-exciton recombination forms a background against which one may attempt to observe the many-exciton recombination processes of interest. This can be done, e.g., using the experiments with several photon detectors operating in the coincidence mode. The photon angular correlations do not vanish on the coherence time scale of the exciton system. Another way of setting off these processes from the background consists in their stimulation by an external laser field.

When stimulated by the external $N - 1$ laser beams with wavevectors $\mathbf{k}_1, \mathbf{k}_2, \dots, \mathbf{k}_{N-1}$, the coherent $N - 1$ -exciton recombination should manifest itself as a unidirectional emission outgoing with, respectively, recoil momentum and energy

$$\mathbf{k}_N = -\sum_{i=1}^{N-1} \mathbf{k}_i, \quad \omega_N = -\sum_{i=1}^{N-1} \omega_i, \quad \omega_i \equiv \omega_{\mathbf{k}_i} \quad (2)$$

from the exciton system. This effect will be referred to as (laser-)stimulated coherent N -exciton recombination (Fig. 2).

In the stimulated coherent N -exciton recombination, the rate of coherent emission with recoil momentum (2) increases (compared to the rate of spontaneous N -exciton recombination in the same direction) by a factor of $\prod_{i=1}^{N-1} (N_i + 1)$, where N_i is the average number of quanta in the inducing laser mode with momentum \mathbf{k}_i . At the same time, the luminescence intensity caused by one-exciton recombination in direction (2) remains unchanged, because the only photon that undergoes stimulated emission belongs to the laser mode $\mathbf{k}_i \neq \mathbf{k}_N$.

Laser radiation contains a great many quanta in the mode. For definiteness, we take 10^3 photons in a mode.² The intensity of induced coherent emission may exceed the background intensity (spontaneous one-exciton recombination), if the following inequality is fulfilled:

$$10^{3(N-1)} W_N > W_1. \quad (3)$$

In what follows, this inequality will serve as a criterion for experimental observation of the stimulated N -exciton recombination effects. Thus, all we need is to estimate W_1 and W_N .

² Modern lasers contain up to 10^5 quanta in a mode.

Let us consider the exciton system at zero temperature. The system is assumed to be in quasi-equilibrium with respect to the exciton–exciton interactions. The exciton–photon and exciton–phonon interactions are assumed to be weak and, thus, will be considered perturbatively. The normal and anomalous Green’s functions of the exciton system can be written as

$$G_{\mathbf{k}}(\omega) = \frac{\omega + \sqrt{\varepsilon_{\mathbf{k}}^2 + \tilde{\mu}^2}}{(\omega - (\varepsilon_{\mathbf{k}} - i\eta_{\mathbf{k}}))(\omega + (\varepsilon_{\mathbf{k}} - i\eta_{\mathbf{k}}))},$$

$$F_{\mathbf{k}}(\omega) = -\frac{\tilde{\mu}}{(\omega - (\varepsilon_{\mathbf{k}} - i\eta_{\mathbf{k}}))(\omega + (\varepsilon_{\mathbf{k}} - i\eta_{\mathbf{k}}))}.$$

Here, $\tilde{\mu} = \rho_{\text{cond}}U_0$, $\varepsilon_{\mathbf{k}} = (\tilde{\mu}k^2/m + (k^2/2m)^2)^{1/2}$, U_0 is the zero Fourier component of the exciton–exciton interaction potential, and m is electron mass.

The direct electron–hole recombination in Cu_2O is a very weak process, and the exciton mainly recombines with the creation of both a photon and an optical phonon. The interaction operator for this process has the form

$$\hat{V}_{ex-ph\ell-phn}(t) = \sum_{\mathbf{p}, \mathbf{q}} \frac{L_{\mathbf{p}, \mathbf{q}}}{\sqrt{V}} \hat{c}_{\mathbf{p}+\mathbf{q}}^\dagger e^{i\omega_{\mathbf{p}+\mathbf{q}}t} \hat{a}_{\mathbf{p}}(t) \hat{\phi}_{\mathbf{p}}(t) + \text{H.c.}, \quad (4)$$

$$\hat{\phi}_{\mathbf{q}}(t) = (\hat{b}_{\mathbf{q}} e^{-i\Omega t} + \hat{b}_{-\mathbf{q}}^\dagger e^{i\Omega t}),$$

where a , b , and c are the exciton, phonon, and photon operators, respectively; Ω is the energy of optical phonons (for simplicity, their dispersion is ignored); L is the effective interaction constant; and V is the volume of the system.

The phonon Green’s function is taken as

$$\mathcal{G}_{\mathbf{q}}(\omega) \equiv \mathcal{G}(\omega) = \frac{2\Omega}{(\omega - (\Omega - i\gamma))(\omega + (\Omega - i\gamma))}.$$

The energy of optical phonons in Cu_2O is $\Omega \approx 10^{-2}$ eV. We take for numerical estimates $\gamma = 10^9$ s $^{-1}$; i.e., the phonon lifetime is assumed to be 10^{-9} s.

The matrix element for the three-exciton recombination also contains the exciton–phonon vertex (Fig. 1b). The operator of this interaction is

$$\hat{V}_{ex-phn}(t) = \sum_{\mathbf{p}, \mathbf{q}} \frac{g_{\mathbf{p}, \mathbf{q}}}{\sqrt{V}} \hat{a}_{\mathbf{p}+\mathbf{q}}^\dagger(t) \hat{a}_{\mathbf{p}}(t) \hat{\phi}_{\mathbf{q}}(t) + \text{H.c.} \quad (5)$$

For simplicity sake, both coupling constants \mathbf{g} and L in Eqs. (4) and (5) are assumed to be independent of the momenta \mathbf{p} and \mathbf{q} ; i.e., $g_{\mathbf{p}, \mathbf{q}} \equiv g$ and $L_{\mathbf{p}, \mathbf{q}} \equiv L$. Numerical estimates will be carried out with $g = 10^2 L$. This corresponds to the intensity of exciton–phonon interaction almost four orders of magnitude higher than the intensity of the exciton–photon–phonon interaction.

The exciton radiative lifetime τ caused by the one-exciton recombination process (Fig. 1a) is

$$\tau^{-1} = L^2 k_0^2 / \pi c. \quad (6)$$

The lifetime $\tau \approx 10$ μs found in Cu_2O corresponds to $L \approx 2.5 \times 10^2$ s $^{-1}$ cm $^{3/2}$. The corresponding spontaneous photon emission rate in a unit volume of the exciton system is $W_1 = \rho_{\text{cond}}\tau^{-1}$.

The spontaneous N -exciton recombination rate in a unit volume of the exciton system can be written as

$$W_N = N \int 2\pi\delta\left(\sum_{i=1}^N \omega_i\right) \times |\mathcal{M}_N(\mathbf{k}_1 \dots \mathbf{k}_N)|^2 V^N \prod_{i=1}^{N-1} \frac{d^3\mathbf{k}_i}{(2\pi)^3}, \quad (7)$$

where \mathcal{M}_N is the matrix element of this process, and the multiplier N allows for the fact that each N -exciton recombination elementary event creates N photons. The matrix element N involves N multipliers $V^{-1/2}$, so that the volume of the system, as expected, does not appear in the final expression for W_N . Below, we set $V = 1$.

The three-exciton recombination matrix element is the sum of expressions obtained from Fig. 1b by transposing the arguments of photon lines:

$$\mathcal{M}_3(\mathbf{k}_1, \mathbf{k}_2, \mathbf{k}_3) = gL^3 \rho_{\text{cond}}^{3/2} \sum_{i \neq j} \mathcal{G}(\omega_i) \mathcal{G}(\omega_j) G_{-\mathbf{k}}(\omega_j), \quad (8)$$

$$i, j = 1, 2, 3.$$

When integrating over momenta and frequencies, the main contribution to the rate of the process comes from the resonance regions, where the arguments of Green’s functions are close to the corresponding poles. In these regions, the photon energies differ weakly from the exciton chemical potential. Indeed, this difference is equal either to the phonon energy or to the energy of elementary excitations in the exciton system. These values are sizably smaller than μ [see Eq. (10)]. For this reason, the absolute values of photon wavevectors can be set equal to k_0 .

In Eq. (8), the momentum k_j can be replaced by k_0 , because matrix element (8) is a function of only the photon energy. Setting $\gamma \ll \Omega$ and $\eta \ll \varepsilon_{k_0}$, one can use

the pole approximation and retain in $|\mathcal{M}|^2$ only six resonant terms, which, in turn, make identical contributions

$$|\mathcal{M}_3(\omega_1, \omega_2, \omega_3)|^2 = 6g^2 L^6 \rho_{\text{cond}}^3 |\mathcal{G}(\omega_2) \mathcal{G}(\omega_1) G_{k_0}(\omega_1)|^2.$$

In the fixed photon wavenumber approximation, the following change of integration measure is possible in Eq. (7):

$$\int \dots 2\pi\delta\left(\sum_{i=1}^3 c(k_i - k_0)\right) \prod_{i=1}^2 \frac{k_i^2 d\omega_i d\cos\theta_i d\phi_i}{c(2\pi)^3} \\ \rightarrow \frac{k_0^3}{\pi c^3} \int \dots \prod_{i=1}^2 \frac{d\omega_i}{(2\pi)}.$$

The role of energy-conserving δ function amounts to fixing the relative directions of photon wavevectors with the same length. Namely, the angles they form with each other are equal to $2\pi/3$.³

Taking this into account, one gets

$$W_3 = 18 \frac{g^2 L^6 \rho_{\text{cond}}^3 k_0^3}{\pi c^3} \\ \times \int |\mathcal{G}(\omega_1) G_{k_0}(\omega_1)|^2 \frac{d\omega_1}{2\pi} \int |\mathcal{G}(\omega_2)|^2 \frac{d\omega_2}{2\pi}.$$

The energy of optical phonons $\Omega = 10^{-2}$ eV far exceeds the energy $\varepsilon_{k_0} \approx 10^{-4}$ eV of elementary excitations in the exciton system. This allows one to simplify the expression for W_3 :

$$W_3 = 18 \frac{g^2 L^6 \rho_{\text{cond}}^3 k_0^3}{\pi c^3} \frac{1}{\Omega^2 \gamma} \left(\frac{1}{\gamma} + \frac{1}{\eta} \left(1 + \frac{\tilde{\mu}^2}{2\varepsilon_{k_0}^2} \right) \right) \\ = 18 \frac{g^2 L^4 \rho_{\text{cond}}^2 k_0^2}{c^2 \Omega^2 \gamma} \left(\frac{1}{\gamma} + \frac{1}{\eta} \left(1 + \frac{\tilde{\mu}^2}{2\varepsilon_{k_0}^2} \right) \right) W_1. \quad (9)$$

The numerical estimates were carried out with the following values for Cu_2O : $m \approx 2.7m_e$, $\tilde{\mu} \approx 0.5$ meV (0.8×10^{12} s⁻¹), $\rho_{\text{cond}} = 10^{19}$ cm⁻³, and $\eta \approx 0.1\tilde{\mu}$. The dielectric constant of Cu_2O is $\varepsilon \approx 9$, $c = c_0/\sqrt{\varepsilon} \approx 10^{10}$ cm/s, and $E_g \approx 2$ eV, so that $k_0 \approx 3 \times 10^5$ cm⁻¹. In this case, the spontaneous three-exciton recombination rate is estimated at $W_3 \approx 10^{-2}W_1$; i.e., approximately every hundredth exciton decay is due to this process. Comparing with Eq. (3), we conclude that this process, when stimulated by external laser beams, can be observed experimentally.

The major contribution to the rate of process (9) comes from the resonance regions, where the intermediate particles are close to their mass surfaces (poles of

³ It follows from the adopted approximations that the angles between the correlated photons may differ from $2\pi/3$ by a small value $\Omega/E_g \approx 5 \times 10^{-3}$.

the corresponding Green's functions). These regions correspond to three sets of photon energies:⁴

$$(\mu + \Omega, \mu - \Omega, \mu), \\ (\mu + \Omega, \mu \pm \varepsilon_{k_0}, \mu - \Omega \mp \varepsilon_{k_0}), \quad (10) \\ (\mu - \Omega, \mu \mp \varepsilon_{k_0}, \mu + \Omega \pm \varepsilon_{k_0}).$$

The first set corresponds to the first term in the parentheses in Eq. (9), i.e., to the process where the intermediate phonon is resonant; whereas the second and the third sets correspond to the second term, i.e., to the process where the elementary excitation of exciton system is resonant. To enhance intensity of the induced three-exciton recombination, the frequencies of inducing laser beams should be equal to any two values from any set in Eq. (10). In this case, the frequency of outgoing radiation is equal to the remaining frequency from the chosen set. In the case of four-exciton recombination, the matrix element is given by

$$\mathcal{M}_4(\mathbf{k}_1 \dots \mathbf{k}_4) = \rho_{\text{cond}} L^4 \\ \times \sum_{l \neq m, m \neq n, n \neq l} F_{-(\mathbf{k}_l + \mathbf{k}_m)}(-(\omega_l + \omega_m)) \mathcal{G}(-\omega_l) \mathcal{G}(-\omega_m), \\ l, m, n = 1 \dots 4.$$

It consists of 12 diagrams obtained from the diagram in Fig. 1c through all inequivalent transpositions of the photon ends. This diagram involves explicitly only two incoming exciton lines. The remaining two incoming excitons are contained in the anomalous Green's function, which is, physically, a diagram for the scattering of two condensate excitons into two noncondensate ones with opposite momenta and energies.

In the pole approximation, one can retain only 12 resonant terms in $|\mathcal{M}_4|^2$. After integration in Eq. (7), they give identical contributions,

$$|\mathcal{M}_4|^2 = 12 \rho_{\text{cond}}^2 L^8 |F_{|\mathbf{k}_1 + \mathbf{k}_2|}(\omega_1 + \omega_2) \mathcal{G}(\omega_1) \mathcal{G}(\omega_3)|^2.$$

In the fixed photon wavenumber approximation, the integration measure in Eq. (7) can be replaced by

$$\int \dots 2\pi\delta\left(\sum_{i=1}^3 c(k_i - k_0)\right) \prod_{i=1}^2 \frac{k_i^2 d\omega_i d\cos\theta_i d\phi_i}{c(2\pi)^3} \\ \rightarrow \frac{k_0^4}{2\pi^2 c^4} \int \dots d|\mathbf{k}_1 + \mathbf{k}_2| \prod_{i=1}^3 \frac{d\omega_i}{(2\pi)}.$$

⁴ In this formula, the chemical potential μ is explicitly included into the photon energy.

This yields the following result for the rate of process:

$$W_4 = 48\rho_{\text{cond}}^2 L^8 \frac{k_0^4}{2\pi^2 c^4} \int \frac{du}{(2\pi)} \times \int_0^{2k_0} dk |F_k(u)|^2 \int \frac{d\omega_1}{(2\pi)} |\mathcal{G}(\omega_1)|^2 \int \frac{d\omega_3}{(2\pi)} |\mathcal{G}(\omega_3)|^2,$$

where $u = \omega_1 + \omega_2$ and $k = |\mathbf{k}_1 + \mathbf{k}_2|$. For a small and k -independent parameter η ($\eta \ll \varepsilon_{k_0}$), the first integral is estimated as

$$\int \frac{du}{(2\pi)} \int_0^{2k_0} dk |F_k(u)|^2 = \frac{\pi \tilde{\mu}^2}{8\eta^2 c_v},$$

where c_v is the velocity of elementary excitations in the exciton system in the linear portion of its spectrum: $c_v = \sqrt{\tilde{\mu}/m}$. With the parameters chosen above, $c_v \approx 0.5 \times 10^6$ cm/s. One finally obtains the following expression for the photon creation rate in the coherent four-exciton recombination process:

$$W_4 = \frac{3\rho_{\text{cond}}^2 L^8 \tilde{\mu}^2 k_0^4}{\pi c_v c^4 \gamma^2 \eta^2} = \frac{3\rho_{\text{cond}} L^6 \tilde{\mu}^2 k_0^2}{c_v c^2 \gamma^2 \eta^2} W_1.$$

With the parameters chosen, one has the following estimate: $W_4 \approx 0.5 \times 10^{-2} W_1$. This result indicates that approximately every hundredth exciton spontaneously decays through this process. Comparing with Eq. (3), we conclude that the stimulated four-exciton recombination can also be detected experimentally.

The mutual spatial orientation of the momenta of four created photons is such that the sum of momenta of any two of them is exactly opposite to the sum of momenta of the remaining two photons. However, the planes in which these two pairs of momenta lie need not be mutually parallel.

As in the case of three-exciton recombination, it is worthwhile remarking that the main contribution to the rate of process comes from the ‘‘resonance’’ regions, where some of the intermediate particles fall on their mass surface. These regions are specified by the following set of photon energies:⁵

$$(\mu + \Omega, \mu - \Omega \pm \varepsilon_{k_0}, \mu - \Omega, \mu + \Omega \mp \varepsilon_{k_0}).$$

To intensify the stimulated four-exciton recombination, the laser frequencies should be equal to any three values from this set. In this case, the frequency of induced emission will be equal to the remaining value from this set.

It should be noted in conclusion that the momentum conservation law plays the crucial role in the effects considered. However, due to the presence of impurities

in the real exciton systems, the exciton momentum acquires uncertainty on the order of $1/l$, where l is the exciton mean free path. It is thus clear that, for the predicted effects to be observed, the inequality $k_0 l \gg 1$ must be fulfilled.

The stimulated N -exciton recombination processes belong to the family of new nonlinear optical effects. Evidently, analogous effects can also be observed in quantum wells (the respective article will be published elsewhere; see also [14]). An alternative method of studying the nonlinear properties of exciton systems is provided by the multiwave-mixing experiments. It should be noted that the physical origins of the stimulated N -exciton recombination and the multiwave mixing (which is used, e.g., for studying the nonlinearities in exciton systems [11, 15]) are essentially different. In particular, in the multiwave mixing, the *wave* in exciton matter is induced by the external laser pump pulses, whereas, in the case of stimulated N -exciton recombination, the Bose-condensed excitons already exist, and the external laser radiations merely induce the recombination processes.

In the processes considered in this work, photons are created coherently. In this case, the state of the photon subsystem is ‘‘squeezed’’ between the photon states with different momenta. One of the classical ways of studying these states is provided by the Hunbury–Brown–Twiss experiments with several photon detectors operating in the coincidence mode.⁶ The use of this approach in studying the exciton systems provides an alternative method for detecting the many-exciton recombination processes. This will be the subject of separate investigation.

Yu.E. Lezovik is grateful to L.V. Keldysh, V.G. Lysenko, and the participants of the ‘‘Nanophotonics-2002’’ workshop for helpful discussions. This work was supported by the Russian Foundation for Basic Research and the program ‘‘Solid State Nanostructures.’’

REFERENCES

1. K. B. Davis, M.-O. Mewes, M. R. Andrews, *et al.*, Phys. Rev. Lett. **75**, 3969 (1995); C. C. Bradley, C. A. Sackett, J. J. Tollett, and R. G. Hulet, Phys. Rev. Lett. **75**, 1687 (1995); M. H. Anderson, J. R. Ensher, M. R. Matthews, *et al.*, Science **269**, 198 (1995).
2. *Bose-Einstein Condensation*, Ed. by A. Griffin, D. W. Snoke, and S. Stringari (Cambridge Univ. Press, Cambridge, 1995).
3. A. L. Ivanov, H. Haug, and L. V. Keldysh, Phys. Rep. **296**, 237 (1998); L. V. Keldysh and Yu. V. Kopaev, Fiz. Tverd. Tela (Leningrad) **6**, 2791 (1964) [Sov. Phys. Solid State **6**, 2219 (1965)]; A. N. Kozlov and L. A. Maximov, Zh. Éksp. Teor. Fiz. **48**, 1184 (1965) [Sov. Phys. JETP **21**, 790 (1965)]; V. A. Gergel, R. F. Kazarinov, and R. A. Suris, Zh. Éksp. Teor. Fiz. **53**, 544 (1967) [Sov.

⁵ The exciton chemical potential μ is explicitly included in this formula [as in Eq. (10)].

⁶ The detectors should be appropriately oriented in space relative to each other and to the exciton system.

- Phys. JETP **26**, 354 (1968)]; B. I. Halperin and T. M. Rice, *Solid State Phys.* **21**, 115 (1968); L. V. Keldysh and A. N. Kozlov, *Zh. Éksp. Teor. Fiz.* **54**, 978 (1968) [*Sov. Phys. JETP* **27**, 521 (1968)]; Yu. E. Lozovik and V. I. Yudson, *Fiz. Tverd. Tela (Leningrad)* **17**, 1613 (1975) [*Sov. Phys. Solid State* **17**, 1054 (1975)]; E. Hanamura and H. Haug, *Phys. Rep.* **33**, 209 (1977); S. A. Moskalenko and D. W. Snoke, *Bose-Einstein Condensation of Excitons and Biexcitons and Coherent Nonlinear Optics with Excitons* (Cambridge Univ. Press, New York, 2000).
4. D. W. Snoke, J. P. Wolf, and A. Mysyrowicz, *Phys. Rev. Lett.* **64**, 2543 (1990); E. Fortin, S. Fafard, and A. Mysyrowicz, *Phys. Rev. Lett.* **70**, 3951 (1993); E. Benson, E. Fortin, and A. Mysyrowicz, *Solid State Commun.* **101**, 313 (1997).
 5. Yu. E. Lozovik and O. L. Berman, *Pis'ma Zh. Éksp. Teor. Fiz.* **64**, 526 (1996) [*JETP Lett.* **64**, 573 (1996)]; Yu. E. Lozovik, O. L. Berman, and V. G. Tsvetus, *Phys. Rev. B* **59**, 5627 (1999); Yu. E. Lozovik and V. I. Yudson, *Pis'ma Zh. Éksp. Teor. Fiz.* **22**, 36 (1975) [*JETP Lett.* **22**, 11 (1975)]; *Zh. Éksp. Teor. Fiz.* **71**, 738 (1976) [*Sov. Phys. JETP* **44**, 389 (1976)]; *Solid State Commun.* **18**, 628 (1976); I. V. Lerner and Yu. E. Lozovik, *Zh. Éksp. Teor. Fiz.* **80**, 1488 (1981) [*Sov. Phys. JETP* **53**, 763 (1981)]; A. V. Klyuchnik and Yu. E. Lozovik, *J. Low Temp. Phys.* **38**, 761 (1980).
 6. L. V. Butov and I. V. Filin, *Phys. Rev. B* **58**, 1980 (1998).
 7. A. V. Larionov, V. B. Timofeev, J. Hvam, and C. Soerensen, *Zh. Éksp. Teor. Fiz.* **117**, 1255 (2000) [*JETP* **90**, 1093 (2000)]; *Pis'ma Zh. Éksp. Teor. Fiz.* **71**, 174 (2000) [*JETP Lett.* **71**, 117 (2000)]; *JETP Lett.* **73**, 342 (2001) [*JETP Lett.* **73**, 301 (2001)].
 8. V. V. Krivolapchuk, E. S. Moskalenko, and A. L. Zhmodikov, *Phys. Rev. B* **64**, 045313 (2001).
 9. Yu. E. Lozovik and A. V. Poushnov, *Phys. Rev. B* **58**, 6608 (1998).
 10. M. Inoue and E. Hanamura, *J. Phys. Soc. Jpn.* **41**, 1273 (1976); H. Shi, G. Verechaka, and A. Griffin, *Phys. Rev. B* **50**, 1119 (1994).
 11. P. Kner, S. Bar-Ad, M. V. Marquezini, *et al.*, *Phys. Rev. B* **60**, 4731 (1999); P. Kner, S. Bar-Ad, M. V. Marquezini, *et al.*, *Phys. Status Solidi A* **164**, 579 (1997).
 12. Yu. E. Lozovik and I. V. Ovchinnikov, *Solid State Commun.* **118**, 251 (2001); Yu. E. Lozovik, I. V. Ovchinnikov, S. Yu. Volkov, *et al.*, *Phys. Rev. B* **65**, 235304 (2002).
 13. I. Loutsenko and D. Roubtsov, *Phys. Rev. Lett.* **78**, 3011 (1997); S. G. Tikhodeev, *Phys. Rev. Lett.* **84**, 3502 (2000); **78**, 3225 (1997).
 14. Yu. E. Lozovik and I. V. Ovchinnikov, *Pis'ma Zh. Éksp. Teor. Fiz.* **74**, 318 (2001) [*JETP Lett.* **74**, 288 (2001)].
 15. K. El Sayed, D. Birkedal, V. G. Lyssenko, and J. M. Hvam, *Phys. Rev. B* **55**, 2456 (1997).

Translated by V. Sakun

Numerical Analysis of Conversion Efficiency in Second-Harmonic Generation in New Crystal CsLiB₆O₁₀¹

L. Wang* and S. Chen**

* Department of Applied Physics, Beijing Polytechnic University, Beijing 100022, China
e-mail: lwang_11cn@yahoo.com

** Institute of Modern Optics, Nan Kai University, Tianjin 300071, China

Received April 8, 2002

In this paper, a detailed theoretical analysis of the second-harmonic generation (SHG) efficiency as a function of polarization ratio and crystal length of CsLiB₆O₁₀ (CLBO) in the phase matching using a computer simulation is presented. The SHG efficiency was as high as 80% when the pumping radiation was a plane wave. The efficiency is 65% and 80% for the pumping waves of type I and type II Gaussian beams, respectively. An important result is that the phase matching of type II is perfectly adopted in the SHG experiment with CLBO. © 2002 MAIK "Nauka/Interperiodica".

PACS numbers: 42.65.Ky

1. A new ultraviolet (UV) nonlinear optical (NLO) crystal CsLiB₆O₁₀ (CLBO) was discovered as a high-power source for solid UV lasers by Y. Mori *et al.* in 1995 [1]. The shortest wavelength transparency of CLBO was found to be at 180 nm [2]. In order to obtain higher output energy and shorter laser wavelength in CLBO, much effort was devoted to up-frequency conversion of the fundamental laser [3–5]. The second-harmonic generation (SHG) is the special case of a three-wave interaction process in the NLO and the Nd:YAG laser was utilized, such as the higher (3rd, 4th, and so on) order harmonic generation [6, 7]. It is important that the numerical analysis of the conversion efficiency of SHG on the NLO CLBO is invested. While BBO was demonstrated to be more effective in recent years, the nonlinear frequency conversion in BBO is limited by its large walk-off angle and relatively small acceptance bandwidths. Recently, the harmonic generation of the picosecond (ps) or nanosecond (ns) Nd:YAG laser output from the SHG to the 5th is also tested in [9]. In this paper, a detailed computer numerical simulation centering the SHG conversion efficiency versus the polarization ratio and the crystal lengths of the CLBO will be introduced in difference pump power on the type I and type II beams. It is based on refractive index data, phase matching (PM) curves, and walk-off angles as a function of fundamental wavelength.

2. Theoretical analysis and computer simulation.

The SHG is a special case of three-wave interaction process in the NLO CLBO. The SHG is based on the second-order nonlinear interaction between the laser fields in an NLO medium with the propagation of three waves in the z direction. The efficiency of the SHG on

CLBO inferred from the Kleinman symmetry and the instantaneous coupled wave equations in the constitutive equations, and the approximations of slowly varied amplitude can be obtained in the incidence of a plane wave and a Gaussian beam.

1. *Plane wave.* The loss of the crystal medium is neglected. The $E_j(z, t)$ form of the incident plane wave

$$E_j(z, t) = E_j(z) \exp i[k_j z - \omega_j t - \Phi_j(z)] \quad (1)$$

$(j = 1, 2, 3),$

where ω_j , k_j , and Φ_j are the frequencies, wave vectors, and initial phase, respectively. The polarization ratio is written as

$$\gamma = \frac{E_2(0) \sqrt{n_2 \cos \alpha_2}}{E_1(0) \sqrt{n_1 \cos \alpha_1}}, \quad (2)$$

where α_i is the walk-off of the corresponding wavelengths. Now let us consider the PM in type I, the conversion efficiency η for $\gamma = 1$ can be written as [1]

$$\eta = \tanh^2(Az), \quad (3)$$

$$A = \left(\frac{8\pi^2 d_{\text{eff}} I_s}{n_1^2 n_2 c \lambda_1^2 \epsilon_0} \right)^{1/2}, \quad (4)$$

where $\tanh(x)$ is the hyperbolic tangent function, I_s is the intensity of pump power, and n_1 and n_2 are the refraction index of the pumping wave and the SHG wave, respectively. Figure 1 shows the PM efficiency curves versus the crystal length, as calculated for type I SHG according to the dispersion equations [1], Eqs. (3) and (4), when the pumped peak power is a scale of 100 MW. We can see clearly from Fig. 1 that the effi-

¹ This article was submitted by the authors in English.

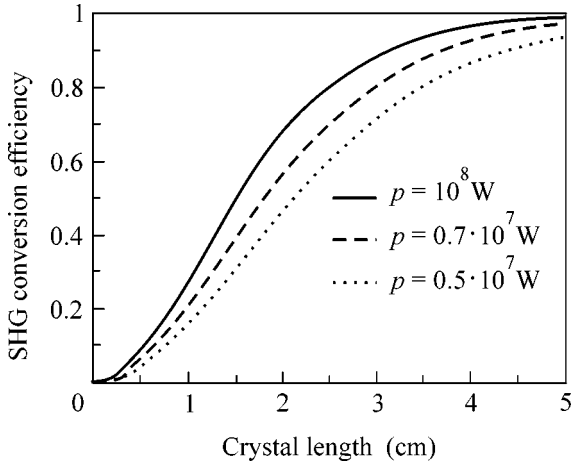


Fig. 1. SHG efficiency curves of type I phase matching for CLBO pumped by the plane wave of 1064 nm.

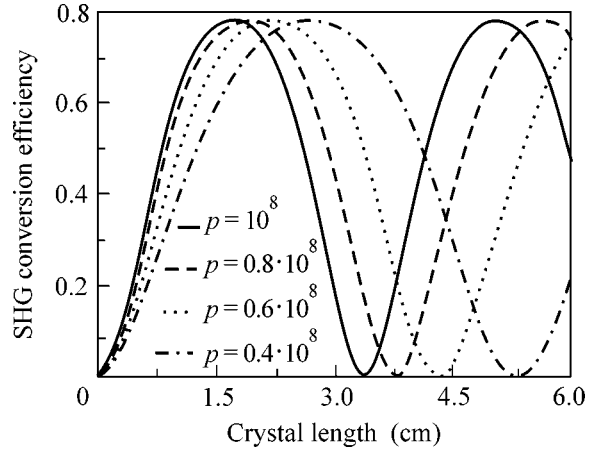


Fig. 2. Curves of SHG conversion efficiency as a function of the crystal length and for $t = 0.8$.

ciency is infinity access to 100% when the optical crystal length increases. But this efficiency will be less than 100% when the phase matching is not realized because of the beam divergence in different directions. When we consider the PM in type I, the efficiency for $\gamma \neq 1$ can reach [10]

$$\eta = \frac{\omega_3 t^2}{\omega_1 + \omega_2 t^2} \text{sn}^2 \left(\sqrt{\frac{1}{\omega_1 + \omega_2 t^2}} Bz, t \right) \quad (t < 1), \quad (5)$$

$$\eta = \frac{\omega_3 t'^2}{\omega_2 + \omega_1 t'^2} \text{sn}^2 \left(\sqrt{\frac{1}{\omega_2 + \omega_1 t'^2}} Bz, t' \right) \quad (t' < 1), \quad (6)$$

$$B = \left(\frac{16\pi^3 d_{\text{eff}}^2 I_s}{n_1 n_2 n_3 \lambda_1 \lambda_2 \lambda_3 \epsilon_0} \right)^{1/2}, \quad (7)$$

where $\text{sn}(x, y)$ is Jacobi elliptic function of the first class. The efficiency curves are shown in Fig. 2 when $\gamma = 0.8$, which is calculated for type II according to the dispersion equations of the CLBO and Eqs. (5) and (6). As shown in Fig. 3, we considered the efficiency curves both of the polarization ratio and the crystal lengths with 80 MW. From Fig. 2 and Fig. 3 that the polarization ratio of the pumping wave is access to 1, the SHG efficiency has a higher in a range of the crystal lengths and a fixed pump. The efficiency is up to 80% when $\gamma = 0.8$. A larger pumping intensity and the longer crystal lengths will lead to a higher energy conversion efficiency with a constant polarization ratio of the pumping wave. The higher output and efficiency can be obtained by increasing the crystal lengths and pumping intensity because the smaller the effect of the nonlinear coeffi-

cient [11], the higher the damage threshold and the larger the crystal dimension of the CLBO.

2. *Gaussian distribution.* If a Gaussian beam is written as

$$E_j(z, j) = E_j(z, r) \exp i[K_j z - \omega t - \Phi_j(z)], \quad (8)$$

where $E_j(z, t)$ is a symmetry function for the z axis and is used in separable form. Then, we can get

$$E_j(z, r) = u_j(z) \omega_j(r) \quad (j = 1, 2, 3). \quad (9)$$

Now let us insert a form of (9) to the three-coupled wave equations [12] can be developed as

$$\frac{du_1}{d\xi} = -2u_1 u_2 \omega_2 \sin \theta, \quad (10a)$$

$$\frac{du_2}{d\xi} = \frac{u_1^2 \omega_1^2}{\omega_2} \sin \theta, \quad (10b)$$

$$\begin{aligned} & \frac{d\theta}{d\xi} - \tan \theta \frac{d}{d\xi} [\ln(u_1^2 u_2)] \\ &= \frac{\Delta K}{K} + \frac{1}{2Kk_2 \gamma} \frac{d}{dr} \left[\ln \left(\frac{\omega_2}{\omega_1^{2K_2/K_1}} \right) \right] = \frac{D}{K}, \end{aligned} \quad (10c)$$

$$\xi = \frac{1}{2} \mu_0 \epsilon_0 d_{\text{eff}} \prod_{j=1}^3 \sqrt{\frac{\omega^2}{k_j \cos \alpha_j}} z = Kz, \quad (10d)$$

where $\theta = z\Delta k + \Phi_3 - \Phi_2 - \Phi_1$, $\Delta k = k_3 - k_2 - k_1$, n_j is the light wave refractive index, and ω_1 and ω_2 is the angle frequency of the foundation wave and harmonic wave, respectively. $D = \Delta k + (2\Delta k - 5k_1)/\omega_0^2 k_1 (\Delta k - 2k_1)$,

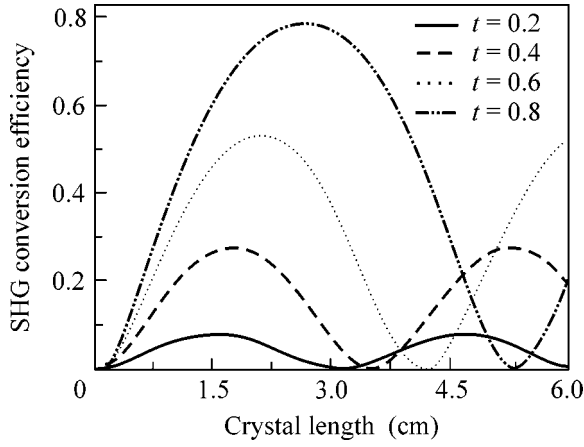


Fig. 3. Curves of SHG conversion efficiency as a function of the crystal length and t , and for $p = 8 \times 10^8$ W.

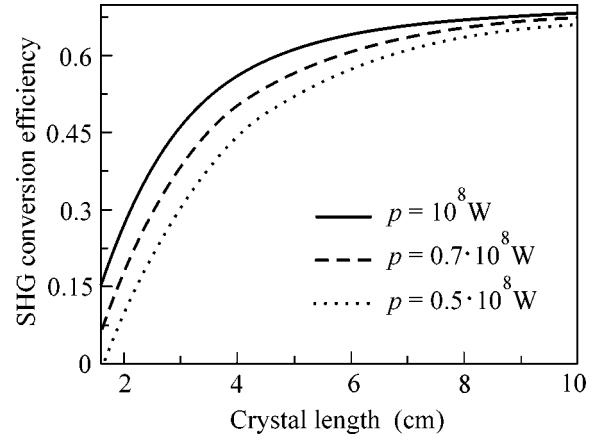


Fig. 4. Efficiency curves of type I SHG versus the length of CLBO pumped by the Gaussian fundamental wave.

where ω_0 is the waist radius of a pumping wave. In order to get the SHG efficiency of type I, we insert

$$\eta = \left| \frac{1}{\sqrt{2}} - \frac{\sqrt{2}}{kzu_0} \tanh(\sqrt{2}kzu_0) + \frac{1}{(kzu_0)^2} \ln[\cosh(\sqrt{2}kzu_0)] \right|, \quad (11)$$

where $u_0 = u_1(0)$. The form of Eq. (11) is the energy conversion efficiency of the CLBO in PM type I. As shown in Fig. 4, we considered the conversion efficiency versus the crystal lengths and used the following typical power parameters: 100 MW, 70 MW, and 50 MW. From Fig. 4, the efficiency is up to 68% when the pumping intensity is larger and the crystal lengths is increasing for type I PM.

For type II PM CLBO, we will use

$$D = \Delta k + \frac{1}{\omega_0^2} \left(\frac{1}{k_1} + \frac{1}{k_2} - \frac{1}{k_3} \right) = 0,$$

in order to get the formula for the efficiency. Then, we can get

$$\eta(z) = \frac{g_1 \gamma^2}{1 + \gamma^2} \times \frac{\int_0^\infty \text{sn}^2 \left[\frac{g_2 E_0(0, r)}{\sqrt{1 + \gamma^2}} z, g_3 \gamma \right] \exp\left(-\frac{r^2}{\omega_0^2}\right) 2\pi r dr}{\int_0^\infty 2\pi r \exp\left(-\frac{r^2}{\omega_0^2}\right) dr} \quad (12a)$$

$(\gamma < 1),$

$\omega_0 = 4$ mm into the form $D = 0$, which leads Δk to be 0, approximately. Then, we can get

$$\eta(z) = \frac{g_1'}{1 + \gamma^2} \times \frac{\int_0^\infty \text{sn}^2 \left[\frac{g_2' E_0(0, r)}{\sqrt{1 + \gamma^2}} z, g_3' / \gamma \right] \exp\left(-\frac{r^2}{\omega_0^2}\right) 2\pi r dr}{\int_0^\infty \exp\left(-\frac{r^2}{\omega_0^2}\right) 2\pi r dr} \quad (12b)$$

$(\gamma > 1),$

where $\gamma = u_2(0)/u_1(0)$ is a polarization ratio,

$$g_1 = \frac{k_2 \omega_3^2 \cos \alpha_2}{k_3 \omega_2^2 \cos \alpha_3}, \quad g_1' = \frac{k_1 \omega_3^2 \cos \alpha_1}{k_3 \omega_1^2 \cos \alpha_3}, \quad (13a)$$

$$g_2 = \frac{1}{2} \mu_0 \frac{d_{\text{eff}} \omega_2 \omega_3}{(k_2 k_3 \cos \alpha_2 \cos \alpha_3)^{1/2}}, \quad (13b)$$

$$g_2' = \frac{1}{2} \mu_0 \frac{d_{\text{eff}} \omega_1 \omega_3}{(k_1 k_3 \cos \alpha_1 \cos \alpha_3)^{1/2}},$$

$$g_3 = \frac{\omega_1 (k_2 \cos \alpha_2)^{1/2}}{\omega_2 (k_1 \cos \alpha_1)}, \quad g_3' = \frac{\omega_2 (k_1 \cos \alpha_1)^{1/2}}{\omega_1 (k_2 \cos \alpha_2)}. \quad (13c)$$

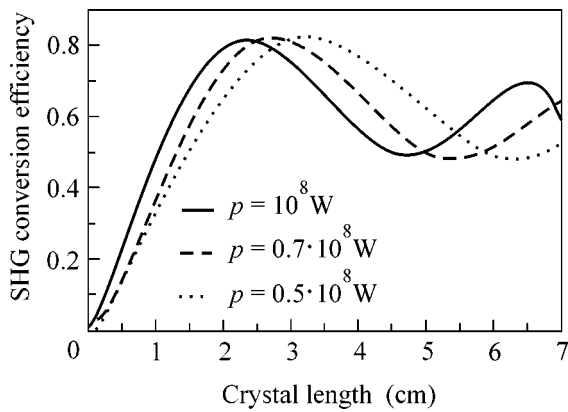


Fig. 5. SHG conversion efficiency curves for CLBO pumped by Gaussian beam and $t = 0.893$.

For type II PM CLBO, which will be used in our theory in order to get the SHG efficiency from the form of (12), we let $g_1 = 2.05$, $g_2 = 0.672 \times 10^{-4}$, $g_3 = 1.008$, and $g_3\gamma = 0.9$, which leads γ to be approximately 0.89. Then, we let the pumping powers be 100 MW, 70 MW, and 50 MW, which leads to the efficiency curves versus the crystal lengths in Fig. 5. From Fig. 5, the efficiency can be up to 80% for type II PM. From Figs. 4 and 5, we can clearly see that the efficiency of type II CLBO is larger than that of type I under the same conditions for a Gaussian beam distribution; type II CLBO is con-

sidered to be ideal for high order harmonic generation, as it follows from our theoretical analysis and computer simulation.

REFERENCES

1. Y. Mori, I. Kuroda, S. Nakajima, *et al.*, Appl. Phys. Lett. **67** (13), 1818 (1995).
2. N. Umemura and K. Kato, Appl. Opt. **36** (27), 6794 (1997).
3. W. R. Bosenberg, L. K. Cheng, and C. L. Tang, Appl. Phys. Lett. **54**, 13 (1989).
4. I. Gontijo, Opt. Commun. **108**, 324 (1994).
5. Y. Mori, I. Kuroda, S. Nakajima, *et al.*, Jpn. J. Appl. Phys. **34** (3A), 296 (1995).
6. Y. K. Yap, S. Haramura, A. Taguchi, *et al.*, Opt. Commun. **145**, 101 (1998).
7. X. F. Wei and W. G. Zheng, High Power Laser and Particle Beams **11** (1), 11 (1999).
8. D. Eimerk, L. Davis, S. Velsko, *et al.*, J. Appl. Phys. **62** (5), 1968 (1987).
9. Y. K. Yap, M. Inagaki, *et al.*, Opt. Lett. **21** (17), 1348 (1996).
10. Y. K. Fan, *Nonlinear Optics* (Jiang Shu Science and Technology Publishing House, Zhejiang, 1989).
11. L. Wang, S. Chen, J. Xue, and Y. Men, Proc. SPIE **4453**, 106 (2001).
12. J. Q. Yao, *Nonlinear Optical Frequency Conversion and Laser Tunable Technology* (Science Publishing House, Beijing, 1995), p. 78.

Spontaneous Transformations of the Magnetic Structure of a Film Nanocontact

A. A. Zvezdin and K. A. Zvezdin

Institute of General Physics, Russian Academy of Sciences, ul. Vavilova 38, Moscow, 119991 Russia

Received April 15, 2002

The magnetization distributions in a symmetric magnetic film nanocontact for oppositely magnetized ferromagnetic electrodes are analyzed based on numerically solving the Landau–Lifshitz and magnetostatic equations as a function of magnetic and geometrical factors. It is found that a symmetric magnetic configuration is unstable when the head-to-head domain wall dividing the regions with opposite orientations of magnetization is located at the center of the nanocontact. The instability arises when the uniaxial magnetic anisotropy constant reaches a certain critical value K_c below which it spontaneously leaves the center of the nanocontact. The transition from the symmetric state (wall at the center) to an asymmetric one can be continuous (second order) or discrete (first order), depending on the geometrical and physical parameters of the nanocontact (length to width ratio, anisotropy constant, and saturation magnetization). The phase diagram is constructed in terms of the variable's nanocontact length vs. anisotropy constant. This diagram divides the symmetric and asymmetric magnetic configurations of the system. The occurrence of a tricritical point in the phase diagram is its characteristic feature. © 2002 MAIK “Nauka/Interperiodica”.

PACS numbers: 75.75.+a; 75.70.Ak; 75.70.Kw

1. The transport properties of nanoscale metal wires and contacts have been the subject of much investigation [1–3]. Quantum jumps of $2e^2/h$, where e is the electron charge and h is the Planck constant, have been observed in electrical conductivity upon varying the thickness of the nanocontact [2, 4, 5]. In the last few years, ferromagnetic nanocontacts and wires have attracted considerable interest in the context of the giant magnetoresistance effect [6–8]. Spin-dependent electron transport through nanowires and contacts with domain walls are also of interest from the viewpoint of the phenomenon of macroscopic quantum tunneling of a domain wall [9] and the effects associated with the Berry phase [7]. The effect of spin accumulation [10, 11] and new effects of magnetization reversal and domain wall displacement induced by a spin-polarized current [12–14] should also be noted in this connection.

Experimental work [15] gave a considerable impetus to investigations of nanocontacts. In this work, a system was investigated that was composed of two macroscopic ferromagnetic rods being connected or disconnected in such a way that a point nanocontact was formed between them at the instant when structure continuity was formed or lost. It was demonstrated that such a system exhibited the effect of giant magnetoresistance that reached several hundreds of percent at room temperature (see also [16–20]).

In spite of the intensive experimental and theoretical investigations of the transport properties of a magnetic nanocontact [15–26], its magnetic structure has been scarcely studied until now. In the analysis of experimental data, it was commonly supposed that the mag-

netizations of ferromagnetic rods are uniform and directed strictly antiparallel to each other. The shape and position of the domain wall in relation to the magnetic and geometrical parameters of the system have not been investigated either. It is evident that all these factors can strongly affect the magnetoresistance of the nanocontact. Micromagnetic modeling is a rather effective method for studying these properties. A micromagnetic study of magnetic configurations arising in nanocontacts that connect bulk rods was carried out in [28]. It was shown that a complex magnetic structure forms in the vicinity of the nanocontact whose main elements are vortex–antivortex pairs in oppositely magnetized regions of the rods adjacent to the contact. Moreover, it was found that, in a number of cases, the head-to-head domain wall is pushed out of the contact; that is, it is localized in one of the electrodes in the vicinity of the contact. The calculated distributions are of importance in understanding the mechanism of the occurrence of giant magnetoresistance and instabilities in the observation of the effect.

It should be noted that nanocontacts with poorly controlled geometry have been used for experiments up to recent time. Thus, work [15] is actually devoted to a statistical study of random nanocontacts formed by the detachment or coupling of two oppositely magnetized rods. It is evident that creating nanocontacts with strictly specified geometrical parameters is necessary for setting up more convincing experiments and for practical use. It is suggested to use film nanostructures for this purpose. This work is devoted to a micromagnetic investigation of such nanostructures.

As was mentioned above, we are interested in nanocontacts of oppositely magnetized electrodes. Such a magnetic configuration is accomplished in a numerical experiment as follows: it is assumed that line conductors are arranged above the ferromagnetic electrodes (beaches), through which oppositely directed current pulses are delivered to induce magnetic fields necessary for the oppositely directed magnetization of the beaches by the head-to-head type. It should be noted that this procedure of creating magnetic head-to-head configurations rather closely models that employed in experiments [15].

2. We present a numerical analysis of the problem obtained by computer micromagnetic modeling. A widespread approach is used in the framework of which a ferromagnet is modeled with the use of a two-dimensional computational grid. Magnetization vectors are specified at the centers of its meshes. To model the quasi-statistics and dynamics of magnetization reversal processes, the magnetodynamic Landau–Lifshitz equations are numerically integrated in each mesh of the computational grid [27],

$$\frac{\partial \mathbf{M}}{\partial t} = \gamma [\mathbf{M} \times \mathbf{H}^{\text{eff}}] - \frac{\alpha \gamma}{M} [\mathbf{M} \times [\mathbf{M} \times \mathbf{H}^{\text{eff}}]], \quad (1)$$

where $\mathbf{M} = \mathbf{M}(x, y)$ is the magnetization vector; M , γ , and α are the saturation magnetization, gyromagnetic ratio, and dissipation constant, respectively; and \mathbf{H}^{eff} is the effective field, which represents a sum of fields of various magnetic interactions,

$$\mathbf{H}^{\text{eff}} = \mathbf{H}^{\text{ext}} + \mathbf{H}^m + \mathbf{H}^{\text{exch-in-layer}}, \quad (2)$$

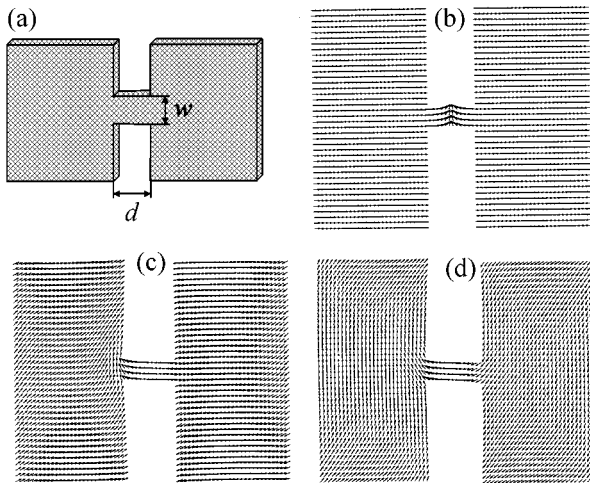


Fig. 1. (a) Nanocontact geometry; (b) magnetization distribution at a high value of the anisotropy constant, the domain wall is at the center of the nanocontact; (c) the domain wall is displaced from the center of the nanocontact; and (d) magnetization distribution at a zero value of the anisotropy constant.

where \mathbf{H}^{ext} is the external magnetic field. The magnetostatic field \mathbf{H}^m , defined by the equation

$$\mathbf{H}^m(\mathbf{r}) = \int_{G_l} \text{div} \mathbf{M}(\mathbf{r}_1) \frac{\mathbf{r} - \mathbf{r}_1}{|\mathbf{r} - \mathbf{r}_1|^3} d\mathbf{r}_1, \quad (3)$$

where \mathbf{r}_1 is the radius vector and G_l is the region under consideration (magnetic surface charges are also taken into account in a standard way), is of the most computational complexity. The main problem is in the long-range character of the magnetostatic interaction; that is, the magnetostatic interaction with all other computational meshes must be recalculated at each time iteration of the solution of Eq. (1) for each computational mesh. We used the fast Fourier transformation method for the acceleration of this procedure.

The other components of \mathbf{H}^{eff} are local and are calculated as follows.

The uniaxial anisotropy field \mathbf{H}^{anis} takes the form

$$\mathbf{H}^{\text{anis}} = \frac{2K}{M^2} (\mathbf{M}, \mathbf{n}) \mathbf{n}, \quad (4)$$

where K and \mathbf{n} are the anisotropy constant and unit vector directed along the easy magnetization axis, respectively; and $\mathbf{H}^{\text{exch-in-layer}}$ is the intralayer exchange field

$$\mathbf{H}^{\text{exch-in-layer}} = \frac{2A}{M^2} \Delta \mathbf{M}, \quad (5)$$

where A is the intralayer exchange constant and Δ is the two-dimensional Laplacian. The following boundary conditions were used:

$$\left. \frac{\partial \mathbf{M}}{\partial \mathbf{N}} \right|_{\partial G} = 0, \quad (6)$$

where \mathbf{N} is the vector normal to the boundary ∂G of the region G .

3. Consider a single-layer ferromagnetic film structure of thickness t composed of two wide platforms connected by a narrow channel of size $d \times w$ (Fig. 1a). Assume that the magnetization and the exchange energy are close to their values in Permalloy, namely, $M_s = 800$ G and $A = 1.25 \times 10^{-6}$ erg/cm. It is assumed that the easy magnetization axis in the film coincides with the x axis. The uniaxial anisotropy constant and the nanocontact length were varied.

The nanostructure in hand (Fig. 1a) is symmetric with respect to the center of the nanocontact; therefore, it may be expected that the boundary between the oppositely magnetized beaches is localized at the center, which is actually accomplished as a result of the action of initial current pulses. We studied the stability of this magnetic configuration after the termination of the action of current pulses creating magnetic fields at the element edges. The results of calculations are reduced to the following. At sufficiently high values of the

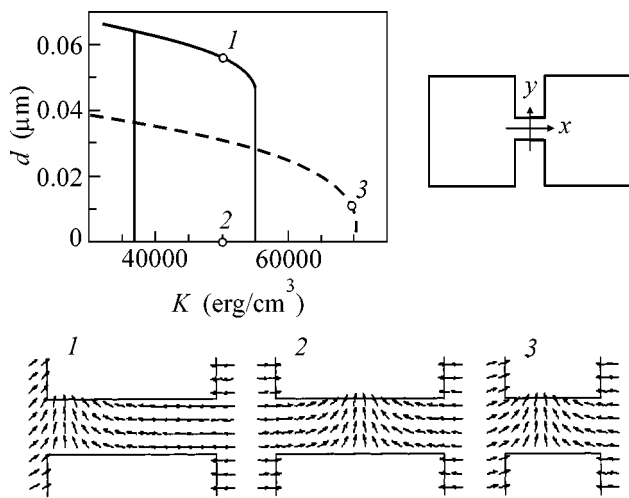


Fig. 2. Dependence of the domain wall position displacement from the center of a long ($wl = 140 \times 40$ nm, solid line) bridge and a short ($wl = 140 \times 40$ nm, dashed line) bridge in a structure of thickness $t = 1$ nm. Shown below are the spin distributions in the nanocontact corresponding to the marked points 1, 2, and 3 of the curves shown in the upper figure.

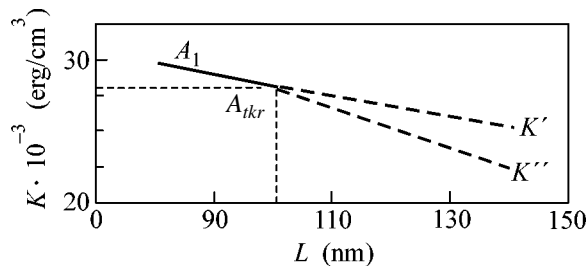


Fig. 3. Phase diagram where the nanocontact length L (nm) and the anisotropy constant (erg/cm^3) are plotted on the axes; the diagram demonstrates the loss of stability of the central position of the domain wall; A_{tkr} is the tricritical point separating the region of parameters at which the domain wall is continuously displaced from the center of the nanocontact from the region of parameters with hysteresis in the displacement of the domain wall.

uniaxial magnetic anisotropy constant, the symmetric magnetic configuration is retained in the system; that is, the equilibrium state corresponds to a domain wall of the head-to-head type located at the center of the nanocontact. As the uniaxial magnetic anisotropy constant decreases, it reaches such a critical value K_c that the domain wall located at the center of the nanocontact loses its stability. For example, $K_c = 5.5 \times 10^4 \text{ erg/cm}^3$ for a bridge of size $140 \times 40 \times 1 \text{ nm}^3$, and $K_c = 7 \times 10^4 \text{ erg/cm}^3$ for a bridge of size $80 \times 40 \times 1 \text{ nm}^3$. Typical magnetization distributions in a nanostructure at $K > K_c$ and $K < K_c$ are shown in Figs. 1b and 1c. As the anisot-

ropy constant further decreases, the magnetization at the adjacent platform ends turns aside perpendicular to the bridge (Fig. 1d).

The phenomenon of spontaneous breaking of the domain wall position symmetry inside the neck of the nanocontact channel described above has an evident analogy with phase transitions at which the system changes its symmetry. The type of the transition depends on the channel length and the anisotropy constant, which is demonstrated well in Fig. 2 by the plots of the deviation of the center of the boundary localization from the middle of the channel as a function of the anisotropy energy.

In the case of a short bridge, the domain wall displacement varies continuously as the anisotropy constant decreases below the critical value (dashed curve) like it takes place in the case of a second-order transition, and a hysteresis curve arises in the case of a long bridge much as for a first-order transition (solid curves in Fig. 2).

Figure 3 displays a phase diagram that determines the regions of existence for these types of domain wall displacement from the center of the nanocontact, depending on the relative values of the anisotropy constant and the nanocontact length. The characteristic tricritical point is shown in the phase diagram. The region of parameters at which the domain wall is continuously displaced from the center of the nanocontact is separated by this point from the region of parameters with hysteresis in the displacement of the domain wall. Line $A_1 A_{tkr}$ corresponds to a continuous transition, and lines $A_{tkr} K'$ and $A_{tkr} K''$ are lines of the loss of stability of the symmetric and asymmetric metastable phase (lability lines). These lines were determined by the calculated hysteresis width.

This work was supported by the Russian Foundation for Basic Research, project no. 02-02-17389; INTAS, project no. 99-01839; and Federal Specialized Program "Physics of Magnetic Nanostructures."

REFERENCES

1. R. Landauer, *Z. Phys. B* **68**, 217 (1987).
2. J. I. Pascual, J. Méndez, J. Gómez-Herrero, *et al.*, *Phys. Rev. Lett.* **71**, 1852 (1993).
3. R. Landauer, *J. Phys.: Condens. Matter* **1**, 8099 (1989).
4. N. Garcia *et al.*, *Europhys. News* **27**, 89 (1996).
5. J. L. Costa-Kramer, N. Garcia, P. Garcia-Mochales, P. A. Serena, M. I. Marques, and A. Correia, *Phys. Rev. B* **55**, 5416 (1997).
6. R. C. Giordano, *Physica B (Amsterdam)* **194**, 1009 (1994); *Phys. Rev. B* **51**, 9855 (1995).
7. Yu. Lyanda-Geller, I. L. Aleiner, and P. M. Goltbart, *Phys. Rev. Lett.* **81**, 3215 (1998).
8. U. Ebels, A. Radulescu, Y. Henry, *et al.*, *Phys. Rev. Lett.* **84**, 983 (2000).
9. C. P. Tataru and Y. Fukuyama, *Phys. Rev. Lett.* **78**, 3773 (1997).

10. M. Johnson and R. H. Silsbee, *Phys. Rev. B* **35**, 4959 (1987); M. Johnson, *Science* **260**, 320 (1993).
11. P. C. van Son, H. van Kempen, and P. Wyder, *Phys. Rev. Lett.* **58**, 2271 (1987).
12. J. C. Slonczewski, *J. Magn. Magn. Mater.* **159**, L1 (1996).
13. L. Berger, *Phys. Rev. B* **54** (13), 9353 (1996).
14. M. V. Tsoi, A. G. M. Jansen, J. Bass, *et al.*, *Phys. Rev. Lett.* **80**, 4281 (1998).
15. N. García, M. Muñoz, and Y.-W. Zhao, *Phys. Rev. Lett.* **82**, 2923 (1999).
16. G. Tatara, Y.-W. Zhao, M. Muñoz, and N. García, *Phys. Rev. Lett.* **83**, 2030 (1999).
17. M. Muñoz, G. G. Qian, N. Karar, *et al.*, *Appl. Phys. Lett.* **79**, 2946 (2001).
18. N. García, M. Muñoz, G. G. Qian, *et al.*, *Appl. Phys. Lett.* **79**, 4550 (2001).
19. N. García, *Appl. Phys. Lett.* **77**, 1351 (2000).
20. N. García, M. Muñoz, and Y.-W. Zhao, *Appl. Phys. Lett.* **76**, 2586 (2000).
21. J. J. Varshni, M. A. Bari, and J. M. D. Coey, *Phys. Rev. Lett.* **87**, 026601 (2001).
22. H. Imamura, N. Kobayashi, S. Takahashi, and S. Maekawa, *Phys. Rev. Lett.* **84**, 1003 (2000).
23. J. M. Coey, L. Berger, and Y. Labaye, *Phys. Rev. B* **64**, 020407 (2001).
24. A. K. Zvezdin and A. F. Popkov, *Pis'ma Zh. Éksp. Teor. Fiz.* **71**, 304 (2000) [*JETP Lett.* **71**, 209 (2000)].
25. L. R. Tagirov, B. P. Vodopyanov, and K. B. Efetov, *Phys. Rev. B* **63**, 104428 (2001).
26. V. V. Osipov, E. V. Ponizovskaya, and N. García, *Appl. Phys. Lett.* **79**, 2222 (2001).
27. L. D. Landau and E. M. Lifshitz, *Course of Theoretical Physics*, Vol. 8: *Electrodynamics of Continuous Media* (Fizmatgiz, Moscow, 1969; Pergamon, New York, 1984).
28. L. L. Savchenko, A. K. Zvezdin, A. F. Popkov, and K. A. Zvezdin, *Fiz. Tverd. Tela (St. Petersburg)* **43**, 1449 (2000) [*Phys. Solid State* **43**, 1509 (2000)].
29. W. F. Brown, *Micromagnetics* (Interscience, New York, 1963; Nauka, Moscow, 1979).

Translated by A. Bagatur'yants

Limiting Rate of Secret-Key Generation in Quantum Cryptography in Spacetime

S. N. Molotkov

*Institute of Solid State Physics, Russian Academy of Sciences,
Chernogolovka, Moscow region, 142432 Russia*

Received April 2, 2002

The fundamental restrictions on the maximum admissible rate of secret-key commitment in quantum cryptography in real time are discussed. It is shown that the maximum rate in a quantum channel with limited transmission band is achieved in a cryptosystem on orthogonal states. The dimensionless rate (the number of bits per unit time frequency band through unit of the channel) is determined by the universal function $C(\lambda_0(\Delta kT))/\Delta kT$ [where $C(\lambda_0(\Delta kT))$ is the transmission capacity of a classical binary channel, Δk is the transmission band width, $1/T$ is the transmission frequency of quantum states, and λ_0 is the maximum eigenvalue of a certain integral equation]. © 2002 MAIK “Nauka/Interperiodica”.

PACS numbers: 03.67.Dd; 03.67.Hk

The problem of the maximum possible rate of secret-key transmission in quantum cryptography is of both fundamental and practical interest. The commitment of the secret key in quantum cryptography requires two communication channels: a quantum channel through which quantum states carrying information about the secret key are transmitted and an open auxiliary classical channel [1]. In this paper, the restrictions imposed by the parameters of the quantum communication channel (in particular, by its transmission band) on the limiting rate of secret-key generation are analyzed. The restrictions on the limiting rate of key generation arise because the states of a quantum system must have carriers in the Minkowski spacetime, in spite of the fact that they are described by vectors (rays) in the Hilbert space \mathcal{H} [2]. In addition, the states in \mathcal{H} should be associated with physical objects (particles), which propagate in the Minkowski spacetime when information is transmitted. The assignment of the basis vectors belonging to different irreducible representations of the Poincaré group in \mathcal{H} to the states of various particles (photons, electrons, etc.) is one of the basic positions in the interpretation of quantum field theory [2].

All quantum cryptosystems can conventionally be divided into three types: systems based on the nonorthogonal states [1], on the Einstein–Podolsky–Rosen effect [3], and on the orthogonal states [4, 5]. The security of the cryptography on nonorthogonal states is based on the impossibility of gaining information about them without their disturbance [1]. In contrast to the nonorthogonal states, the orthogonal states are indistinguishable with certainty if they are entirely accessible for measurement (in fact, the state carrier in the Minkowski spacetime is entirely accessible) and are

indistinguishable with certainty if they are not accessible entirely. Moreover, they remain indistinguishable with certainty even if they are orthogonal in the presence of a restriction on any spacetime region [5].¹ Secret-key commitment protocols on the orthogonal states are organized in such a way that the states propagating through a communication channel are never present entirely in it at the same time [4, 5]. For detecting the eavesdropping attempts in the cryptography on orthogonal states, it is substantial that, according to special relativity, the propagation velocity of quantum states is limited [4, 5]. For the cryptosystems on nonorthogonal states, the spacetime structure of the latter is not taken into account in an explicit form, because the fact that the state vectors in \mathcal{H} are nonorthogonal is formally sufficient for the protocols. In contrast, for the cryptosystems on orthogonal states, the spacetime structure of states is taken into account in an explicit form from the very beginning, because it is the necessary element in commitment protocols.

Below, it will be shown that taking account of the spacetime structure of quantum states leads to the restrictions on the limiting rate of secret-key commitment in a quantum channel with a finite frequency transmission band. These restrictions, in effect, are the same for the cryptographies on nonorthogonal and orthogonal states, if one does not ignore the fact that the information is carried by particular physical objects. Restrictions on the properties of the quantum communication channel always exist. For example, in an optical fiber, restriction is associated with the finiteness of the pass band. For the cryptography through open space, a restriction is imposed by the transparency win-

¹ Note that, in the scheme given in [4], the states in the channel are effectively nonorthogonal, in contrast to [5].

dow in the atmosphere. Therefore, restriction on the transmission band is a rather general thing.

Let us first discuss the restrictions on the limiting rate of key generation for the cryptosystems on nonorthogonal states. The amount of classical information, which can be transmitted from one participant (*A*) of a cryptographic protocol to the other participant (*B*) using quantum states is determined by the maximum of mutual information restricted by the Holevo inequality [6]:

$$I(A; B) = \max_{E_i} \sum_i \left\{ \pi_0 \text{Tr}\{\rho_0 E_i\} \log_2 \left(\frac{\text{Tr}\{\rho_0 E_i\}}{\text{Tr}\{\rho E_i\}} \right) + \pi_1 \text{Tr}\{\rho_1 E_i\} \log_2 \left(\frac{\text{Tr}\{\rho_1 E_i\}}{\text{Tr}\{\rho E_i\}} \right) \right\} \leq S(\rho) - \sum_{i=0,1} \pi_i S(\rho_i), \quad (1)$$

$$S(\rho) = -\text{Tr}\{\rho \log_2 \rho\},$$

where $S(\rho)$ is the von Neumann entropy, $\pi_{0,1}$ are the *a priori* probabilities of sending quantum states $\rho_{0,1}$, $\rho = \pi_0 \rho_0 + \pi_1 \rho_1$ ($\pi_0 + \pi_1 = 1$), and E_i are the measuring operators such that $I = \sum_i E_i$ is the identity operator. Consider pure states $\rho_{0,1} = |\varphi_{0,1}\rangle\langle\varphi_{0,1}|$. In this case, $S(\rho_i) = 0$. The maximum rate of key generation is determined by the transmission capacity of the quantum channel. This capacity is given by the maximum among all possible input *a priori* distributions of mutual information (1) [7] (maximum is reached at $\pi_0 = \pi_1 = 1/2$):

$$C = -\left[\left(\frac{1-\varepsilon}{2} \right) \log_2 \left(\frac{1-\varepsilon}{2} \right) + \left(\frac{1+\varepsilon}{2} \right) \log_2 \left(\frac{1+\varepsilon}{2} \right) \right], \quad (2)$$

$$\varepsilon = |\langle\varphi_0|\varphi_1\rangle|.$$

The quantity C is the amount of information in classical bits (≤ 1) which can be transmitted with an arbitrarily low error in one message for a sufficiently long transmitted sequence [8]. Therefore, the quantity $1/C$ determines the number of messages (rate). These arguments are valid for the case where an eavesdropper is absent. In the presence of an eavesdropper, it is impossible to make any general conclusions about the key-generation rate, because eavesdropping may be so intense that it blocks the key commitment.

The maximum key-generation “rate” (transmission capacity) for the cryptosystems on nonorthogonal states cannot exceed the rate for orthogonal states. To achieve the generation rate equal to the transmission capacity for the nonorthogonal states in the asymptotic limit of large sequences, collective measurements on the blocks of states are required [9] (these measurements amount to the projection onto the subspace of typical sequences). For the orthogonal states, collective measurements are not required. It is sufficient to make individual measurements for the state in each message. The measurement reduces to the tensor product of indi-

vidual measurements, each given by the unity decomposition of the form

$$I = E_0 + E_1, \quad E_{0,1} = |\varphi_{0,1}\rangle\langle\varphi_{0,1}|, \quad (3)$$

where $E_{0,1}$ are the projectors onto the states. The measurement on a sequence of length N is given by the unity decomposition

$$I^{\otimes N} = \overbrace{I \otimes I \dots \otimes I}^N. \quad (4)$$

Measurements consisting in the projection onto either the individual states or their blocks provide no information about the key-generation rate in real time, because projectors do not involve explicit information about the spacetime structure of states. Since all events for observers inevitably occur in the Minkowski spacetime, measurements must involve explicit or implicit information about the spacetime regions. This remark is immaterial in the nonrelativistic quantum mechanics, because the propagation velocity is unlimited. In quantum field theory, one cannot ignore restrictions imposed by special relativity on the limiting propagation velocity of quantum objects.

Below, the vectors $|\varphi_{0,1}\rangle \in \mathcal{H}$ denote the one-photon states, and information is assumed to be coded, as usual, by the polarization states of photons. Within the framework of the “nonrelativistic” quantum-mechanical treatment of photons, which is often used in the problems of the quantum theory of information, the spatial degrees of freedom are, as a rule, ignored and only the polarization degrees of freedom, which are described by the vectors in a Hilbert space with $\dim \mathcal{H} = 2$, are taken into account. Neither the electron spin nor the photon polarization exist independently of the spatial degrees of freedom. Moreover, since the quantized photon field is massless and transverse, the spatial and polarization degrees of freedom, strictly speaking, cannot be represented in the factorized form. For our purposes, it is sufficient to consider a one-dimensional massless particle with two polarization states. Though idealized, this representation reflects the main properties of quasi-one-dimensional optical fibers and narrow light beams. The states of a free massless quantized field are generated by field operators (generalized functions with operator values) [2] acting on the vacuum vector:²

$$\varphi_\mu^+(\hat{x}) = \frac{1}{\sqrt{2\pi}} \int (d\hat{k}) \delta(\hat{k}^2) \theta(k_0) e^{i\hat{k}\hat{x}} a_\mu^+(k),$$

$$\hat{k} = (k, k_0), \quad \hat{x} = (x, t), \quad d\hat{k} = dk dk_0, \quad (5)$$

$$\hat{k}\hat{x} = kx - k_0 t, \quad [a_\nu^-(k), a_\mu^+(k')] = k_0 \delta(k - k') \delta_{\nu,\mu}.$$

² Strictly speaking, the generalized operator functions must satisfy the Maxwell equations $id\varphi/dt = -\nabla \times \varphi$ and $\nabla \cdot \varphi = 0$.

The subscripts $\mu, \nu = 0, 1$ number two basis polarization states. The physical states $|\varphi_m\rangle \in \mathcal{H}$ of a quantized field are obtained by smoothing out the generalized operator functions with the basic functions $\varphi(\hat{x}) \in \Omega(\hat{x})$ [$\Omega(\hat{x})$ is the space of basic functions [2]]; $\varphi_\mu^+(\hat{x})|0\rangle \in \Omega(\hat{x})^*$ are the generalized eigenvectors (linear continuous functionals in \mathcal{H}); $\Omega(\hat{x}) \subset \mathcal{H} \subset \Omega^*(\hat{x})$ is the equipped Hilbert space (Gelfand triad) [10]; and

$$\begin{aligned} |\varphi_\mu\rangle &= \int d\hat{x} \varphi(\hat{x}) \varphi_\mu^+(\hat{x})|0\rangle = \int d\hat{k} \tilde{\varphi}(\hat{k}) \delta(\hat{k}^2) \theta(k_0) a_\mu^+(k)|0\rangle \\ &= \int_{-\infty}^{\infty} \frac{dk}{k_0} \tilde{\varphi}(k, k_0 = |k|) |k, \mu\rangle, \end{aligned} \quad (6)$$

$$|k, \mu\rangle = a_\mu^+(k)|0\rangle, \quad \langle k', \nu | k, \mu\rangle = k_0 \delta_{\mu, \nu} \delta(k - k').$$

The normalization condition is

$$\begin{aligned} \langle \varphi_\mu | \varphi_\mu \rangle &= \int_{-\infty}^{\infty} \frac{dk}{k_0} |\tilde{\varphi}(k, k_0 = |k|)|^2 = \int_{-\infty}^{\infty} dk |\varphi(k)|^2 = 1, \\ \varphi(k) &= \frac{\tilde{\varphi}(k, k_0 = |k|)}{\sqrt{k_0}}. \end{aligned} \quad (7)$$

The states are assumed to differ only in the polarization and have the same spatial amplitude $\tilde{\varphi}(\hat{k})$. The states $|\varphi_\mu\rangle$ are determined by the amplitude $\tilde{\varphi}(\hat{k})$ on the mass surface $k_0 = |k|$. If the information is transmitted between two participants, it is reasonable to consider the states propagating in one direction ($k > 0$). In this case, all quantities depend on the difference $\tau = x - t$, i.e., on the variable on one of the light-cone branches.

A measurement distinguishing with certainty between a pair of orthogonal states is given by unity decomposition (2) in the one-particle subspace of states. The projectors inevitably include the spatial component of the state vector. The states are distinguished with certainty if the entire state [spatial region where the state amplitude $\varphi(x, t)$ is nonzero] is accessible. Formally, the amplitude is nonzero in the whole space. This fact follows from the Wiener–Palley theorem [11]: the Fourier transform of a normalized function $\varphi(k)$ ($k \geq 0$),

$$\int_0^{\infty} dk |\varphi(k)|^2 = 1, \quad (8)$$

equal to zero in the $k < 0$ semiaxis, but not identically

equal to zero must satisfy the condition

$$\begin{aligned} \int_{-\infty}^{\infty} \frac{\ln|\varphi(\tau)|}{1 + \tau^2} d\tau < \infty, \\ \varphi(\tau) = \int_0^{\infty} dk e^{-k\tau} \varphi(k), \quad \tau = x - t. \end{aligned} \quad (9)$$

As follows from Eq. (9), the state amplitude cannot decrease exponentially but can decrease at infinity arbitrarily close to the exponential $|\varphi(\tau)| \propto e^{-\alpha|\tau|/\ln(\ln(\ln(\dots\ln|\tau|)))}$, where $\alpha > 0$ can be as large as desired.

The real measurements cannot cover the whole space; the access to the whole space would require infinite time because of the existence of the limiting velocity. If measurement is carried out in a finite accessible region, the space of results is $\Theta = (\Omega \times (0, 1) \cup \bar{\Omega})$, where Ω is the region accessible for detection, $\mu = (0, 1)$ label the channels for the orthogonal polarization states, and the region $\bar{\Omega}$ is inaccessible for the measurement.

$$\begin{aligned} I &= \bigoplus_{\mu=0,1} \int_{\Delta k} \frac{dk}{k} |k, \mu\rangle \langle \mu, k| \\ &= \bigoplus_{\mu=0,1} (\mathcal{M}(\Omega, \mu) + \mathcal{M}(\bar{\Omega}, \mu)), \end{aligned} \quad (10)$$

where

$$\mathcal{M}(\Omega, \mu) = \int_{\Omega} \mathcal{M}(d\tau, \mu), \quad (11)$$

$$\mathcal{M}(\bar{\Omega}, \mu) = \int_{\bar{\Omega}} \mathcal{M}(d\tau, \mu), \quad \bar{\Omega} \cup \Omega = (-\infty, \infty),$$

$$\begin{aligned} \mathcal{M}(d\tau, \mu) &= \left(\int_{\Delta k} \frac{dk}{\sqrt{k}} e^{ik\tau} |k, \mu\rangle \right) \\ &\times \left(\int_{\Delta k'} \frac{dk'}{\sqrt{k'}} e^{-ik'\tau} \langle k', \mu| \right) \frac{d\tau}{2\pi}. \end{aligned} \quad (12)$$

Unity decomposition (12) is the formal description of an instrument; it can be interpreted as follows. If the spatial regions x are considered as the space of results, a measurement should be treated as an instrument distributed over x and generating random outcome in the vicinity of a certain point $(x, x + dx)$ at time t . If x is fixed (local instrument), a measurement describes an instrument operating in the waiting regime and generating the outcome at a random time instant $(t, t + dt)$. The fact that the operator measure $\mathcal{M}(d\tau, \mu)$ depends only on the difference $\tau = x - t$ (coordinate in the left

branch of the light cone) and not on x and t separately, implies that, if an outcome can be obtained with a certain probability in the vicinity of x at time t , it can be obtained with the same probability at another point x' but at time $t' = x' - x + t$. The size of a region accessible on the light cone determines the time it takes for obtaining the final outcome. For brevity, a measurement with outcomes in the accessible region Ω on the light cone will be referred to below as a measurement in the time window $\Omega = (-T, T)$ (the outcome cannot be obtained by an observer faster than in time T [12]). The probability of correct identification of the states with orthogonal polarizations in the time window $(-T, T)$ is equal to [5]

$$\begin{aligned} p &= p(0|0) = p(1|1) \\ &= \frac{1}{2} (1 + \text{Tr}\{\mathcal{M}(\Omega, \mu)|\varphi_\mu\rangle\langle\varphi_\mu|\}) \\ &= \frac{1}{2} \left(1 + \int_{-T}^T |\varphi(\tau)|^2 d\tau \right), \end{aligned} \quad (13)$$

and, correspondingly, the probability of error is

$$\begin{aligned} 1 - p &= p(0|1) = p(1|0) \\ &= 1 - p(0|0) = 1 - p(1|1). \end{aligned} \quad (14)$$

Note that, to distinguish with certainty between two spatially extended classical signals (electromagnetic wave with two orthogonal polarization states), it suffices to use an arbitrarily small region where the signal exists. Since the vector of quantum state is normalized ($\int_{-\infty}^{\infty} |\varphi(x, t)|^2 dx = \int_{-\infty}^{\infty} |\varphi(x, t')|^2 dx = 1$; t and t' are arbitrary), the probability of correctly distinguishing between the locally orthogonal quantum states is proportional to the contribution coming to the normalization integral from the region accessible for measurement. For the same reason, the probability of distinguishing provided by the collective measurements is no higher than the probability provided by the individual measurements.

Since the states are orthogonal (more precisely, locally orthogonal), the transmission capacity is given by the formula for a classical symmetric binary channel:

$$\begin{aligned} C(p) &= 1 - C_H(p), \\ C_H(p) &= -(1 - p) \log_2(1 - p) - p \log_2 p. \end{aligned} \quad (15)$$

If there are no restrictions on the properties of the quantum channel, one can transmit through it the states localized in τ as strongly as desired. In this case, the property that the states can be detected with an arbitrarily small error within an arbitrarily narrow time window $(-T, T)$ means that they can be transmitted with an arbitrarily high rate. More exactly, for any given $T < \varepsilon$ and $\delta > 0$, the state can be chosen in such a way that

the probability of correctly distinguishing will be as close to unity as desired:

$$p = \frac{1}{2} \left(1 + \int_{-T}^T |\varphi(\tau)|^2 d\tau \right) > 1 - \delta, \quad \delta \rightarrow 0. \quad (16)$$

Let the channel transmission band be limited by the energy interval $\Delta\omega = \Delta k$ (speed of light $c = 1$). The position of the transmission window on the energy axis is of no importance. In this case, the problem amounts to finding the optimal form of the state $\varphi(k)$ ($\varphi(\tau)$, for which the maximum transmission capacity $C(p)$ [maximum probability of detecting the state within the time window $(-T, T)$] is reached at a given channel transmission band and chosen transmission rate $1/T$). Thus, it is necessary to find the states maximizing the functional

$$\begin{aligned} \mathcal{F}(|\varphi\rangle) &= \max_{\text{supp}|\varphi\rangle \in \Delta k} \frac{\text{Tr}\{\mathcal{H}(\tau \in (-T, T))|\varphi\rangle\langle\varphi|\}}{\| |\varphi\rangle \|^2} \\ &= \max_{\text{supp}|\varphi\rangle \in \Delta k} \frac{\frac{1}{2\pi} \int_{-T}^T |\varphi(\tau)|^2 d\tau}{\int_{\Delta k} |\varphi(k)|^2 dk}. \end{aligned} \quad (17)$$

By varying the functional, $\delta\mathcal{F}/\delta\varphi = 0$, one arrives at the integral equation

$$\lambda_n \varphi_n(k) = \frac{1}{\pi} \int_{\Delta k} \varphi_n(k') \frac{\sin(k - k')T}{(k - k')} dk'. \quad (18)$$

The maximum eigenvalue and the corresponding eigenfunction give the maximum of the functional and the optimal form of the state, respectively. This equation was analyzed earlier in [13, 14]. The eigenvalues are positive and form a descending sequence ($1 > \lambda_1 > \lambda_2 \dots > 0$, $n = 0, 1, \dots, \infty$). They are functions of the parameter $\Delta k T$. Several first eigenvalues were found numerically in [13] for various values of $\Delta k T$ (the eigenvalues tend rapidly to unity with increasing parameter $\Delta k T$; e.g., $\lambda_0 = 0.99589$ for $\Delta k T = 4$). For a fixed number n , the asymptotic behavior at $\Delta k T \rightarrow \infty$ is also known [14]:

$$\lambda_n(c) \sim 1 - \frac{4\sqrt{\pi} 8^n}{n!} c^{n+1/2} e^{-2c}, \quad c = \Delta k T, \quad (19)$$

i.e., the eigenvalues are exponentially close to unity. The latter means that the error of distinguishing between the orthogonal states is exponentially small for a wide time window ($T \gg 1/\Delta k$), and the channel transmission capacity is exponentially close to unity.

According to the standard treatment of transmission capacity, the latter means that one can always find a random code with transmission rate R as close to C as desired, but $R < C$, which allows information of C clas-

sical bits to be transmitted per one message with an arbitrarily small error for a sufficiently long sequence. In this case, each message and measurement occurs with the rate $1/T$ in real time. The rate of generating one bit in a key in real time is $C(\lambda_0(\Delta k T))/T$. In actuality, the transmission rate on the nonorthogonal polarization states is always somewhat lower, because the transmission capacity for the nonorthogonal states is always lower than for the orthogonal states (if their spatial forms are identical).

For small parameters $\Delta k T \ll 1$, the eigenvalue is $\lambda_0 \sim \Delta k T$ and the transmission capacity is $C \sim (\Delta k T)^2 \ll 1$.

Let us discuss the key generation rate in a cryptosystem on extended orthogonal states [5]. Since the whole orthogonal state is never present in the communication channel at the same time and the propagation velocity is limited, these states are indistinguishable for an eavesdropper and any eavesdropping attempt can be detected. At first glance, it may appear that the key generation in real time is slower, because one is led to use the states having extended carriers in spacetime. However, it proves that the theoretical maximum of secret-key generation for a given transmission band of a quantum communication channel is achieved for a cryptosystem on extended orthogonal states rather than for a cryptosystem on nonorthogonal states. Before proving this statement, we present some heuristic arguments. The length of a state cannot be less than the channel length $L_{\text{ch}} = cT_{\text{ch}}$ [5]. Therefore, this must be a sufficiently narrow-band state ($\Delta k_{\text{ch}} < 1/T_{\text{ch}}$). For a given transmission band Δk , N states with orthogonal polarizations and nonoverlapping carriers in the k space ($N \sim \Delta k/\Delta k_{\text{ch}}$) can be transmitted simultaneously. The detection of each state requires a time window no smaller than T_{ch} , but, in this case, N states are simultaneously transmitted through independent channels. The physical time per key bit is $T \sim NT_{\text{ch}} = N/\Delta k_{\text{ch}} = N/N\Delta k$, which coincides with the preceding result. The frequency band Δk can be divided into an arbitrary number of independent channels; the only requirement is that the band of each channel be narrow enough ($\Delta k_{\text{ch}} < 1/T_{\text{ch}}$). In fact, this division is analogous to multiplexing in the classical case. In this case, the channel is a set of N independent channels, each having the transmission band δk_i ($\delta k_i \cap \delta k_j \neq \emptyset \cup_i \delta k_i = \Delta k$). In what follows, all δk_i are assumed to be identical. N states $\{|\varphi_{\mu}^i\rangle\}$, where $|\varphi_{\mu}^i\rangle = \int_{\delta k_i} dk \varphi(k)|k, \mu\rangle$, are simultaneously sent into each channel.

The unity decomposition describing a measurement in the subspace spanned by the generalized vectors

$|k, \mu\rangle$, $k \in \Delta k$ has the form

$$I(\Delta k) = \bigoplus_{i=1, \dots, N} I(\delta k_i), \quad (20)$$

$$I(\delta k_i) = \bigoplus_{\mu=0,1} \int_{\delta k_i} \frac{dk}{k} |k, \mu\rangle \langle \mu, k|.$$

where the detecting operators for each channel are

$$I(\delta k_i) = \bigoplus_{\mu=0,1} (\mathcal{M}_i(\Omega_{\delta}, \mu) + \mathcal{M}_i(\bar{\Omega}_{\delta}, \mu)), \quad (21)$$

$$\Omega_{\delta} = (-T_{\delta}, T_{\delta}), \quad \bar{\Omega}_{\delta} = (-\infty, \infty) - \Omega_{\delta},$$

$$\begin{aligned} & \mathcal{M}_i(\Omega_{\delta}, \mu) \\ &= \int_{-T_{\delta}}^{T_{\delta}} \frac{d\tau}{2\pi} \left(\int_{\delta k_i} dk e^{ik\tau} |k, \mu\rangle \right) \left(\int_{\delta k_i} dk' \langle \mu, k'| e^{-ik'\tau} \right) \end{aligned} \quad (22)$$

and similarly for $\mathcal{M}_i(\bar{\Omega}_{\delta}, \mu)$. The probability of correct identification of the states in each channel in time window $(-T_{\delta}, T_{\delta})$ is given by

$$\begin{aligned} p_i &= p(0_i|0_i) = p(1_i|1_i) \\ &= \frac{1}{2} (1 + \text{Tr}\{\mathcal{M}_i(\Omega_{\delta}, \mu)|\varphi_{\mu}^i\rangle \langle \varphi_{\mu}^i|\}) \\ &= \frac{1}{2} (1 + \lambda_0(\delta k_i T_{\delta})), \end{aligned} \quad (23)$$

where 0_i and 1_i correspond, respectively, to 0 and 1, for each channel. The maximal p_i (and, therefore, the minimal error) in each channel is reached for the states maximizing the functional analogous to (17) with replacements $\Delta k \rightarrow \delta k_i$ and $T \rightarrow T_{\delta}$.

Since the eigenvalues of integral Eq. (18) depend only on the product of the transmission band by the time window, the total transmission capacity through all N independent channels is

$$\sum_{i=1}^N C(\lambda_0(\delta k_i T_{\delta})) = NC(\lambda_0(\delta k_i T_{\delta})). \quad (24)$$

Since the transmission bands of individual channels are identical, $\delta k_i = \Delta k/N$, and the upper bound δk_i is determined by the length of the communication channel, one can conclude, after choosing the time window $T_{\delta} = TN$, that the transmission, with an arbitrarily small error, of one secret bit through one of the channels requires, for a sufficiently long sequence, the physical time

$$T_N = \frac{TN}{NC(\lambda_0(\delta k_i T_{\delta}))} = \frac{T}{C(\lambda_0(\Delta k T))}. \quad (25)$$

Since the states can be transmitted simultaneously through N independent channels, one bit requires the

time $T = T_N/N$, which coincides with the preceding result.

The above formulas are asymptotic, since the states in the individual frequency channels or individual messages become orthogonal (distinguishable with certainty) only in the asymptotic limit [correspondingly, the nonorthogonal operator-valued measures $\mathcal{M}(\tau \in (-T, T))$ become the orthogonal projectors $I(\Delta k)$]; i.e.,

$$I(\Delta k) = \lim_{\Delta k T \rightarrow \infty} \bigoplus_{\mu=0,1} \mathcal{M}(\tau \in (-T, T)). \quad (26)$$

However, the limit is attained exponentially fast with respect to the parameter $\Delta k T$. For this reason, the formulas for the channel transmission capacity can be used even at $\Delta k T \approx 2$. Since the transmission capacity depends only on $\Delta k T$, it is more convenient to introduce a dimensionless quantity $C(\lambda_0(\Delta k T))/\Delta k T$, which can be treated as the number of bits per unit time through unit frequency band. The values of this quantity are presented below for several values of parameter $\Delta k T$ (the eigenvalues λ_0 are taken from the numerical calculations in [12]). For large $\Delta k T \approx 2$, the transmission capacity is exponentially close to $C(\lambda_0(\Delta k T))/\Delta k T \approx 1/\Delta k T$:

$\Delta k T$:	0.5	1.0	2.0	4.0
$\frac{C(\lambda_0(\Delta k T))}{\Delta k T}$:	0.14067	0.25148	0.33684	0.24467.

In the case that the spatial amplitudes of states overlap in sequential messages, the expression for key-generation rate cannot be obtained without considering a particular model of quantum communication channel.

As with the cryptography on orthogonal states, one can use nonorthogonal states with extended carriers (with an arbitrary effective length, either smaller or larger than the communication channel length), which are transmitted simultaneously though the communication channel in the multiplex regime. In this case, the limiting rate of key generation will be determined by the same expression, because it depends only on the product $\Delta k T$, and will be lower than the rate for orthogonal states.

In conclusion, note that the expression $C(\lambda_0(\Delta k T))/\Delta k T$ for the dimensionless rate of secret-key generation is Lorentz-invariant (is the same in different inertial frames of reference), which can be rigorously proved as in [15]. This follows from the Lorentz invariance of the scalar product $\hat{k}\hat{x} = kx - k_0t$ ($c = 1$, $k_0 = |k|$) for a photon propagating in one direction $k_0 =$

k ($k > 0$). In the other inertial frame of reference, one has $k' = (k - \beta k_0)/\sqrt{1 - \beta^2} = k\sqrt{(1 - \beta)/(1 + \beta)}$, and $T' = (x + \beta t)/\sqrt{1 - \beta^2} - (t + \beta x)/\sqrt{1 - \beta^2} = T\sqrt{(1 + \beta)/(1 - \beta)}$, because the time and coordinate for a massless field appear only in the combination $T' = x' - t'$ and $T = x - t$. Therefore, the product $\Delta k T = \Delta k' T'$ is Lorentz-invariant.

I am grateful to K.A. Valiev, S.S. Nazin, Yu.I. Ozhigov, L.A. Fedichkin, and V.N. Yashnikov for discussions and remarks. This work was supported by the Russian Foundation for Basic Research (project no. 02-02-16289) and the project "Kvant" (37.029.1.1.0031).

REFERENCES

1. C. H. Bennett, Phys. Rev. Lett. **68**, 3121 (1992); C. H. Bennett, G. Brassard, and N. D. Mermin, Phys. Rev. Lett. **68**, 557 (1992).
2. N. N. Bogolyubov, A. A. Logunov, A. I. Oksak, and I. T. Todorov, *General Principles of Quantum Field Theory* (Nauka, Moscow, 1987).
3. A. K. Ekert, Phys. Rev. Lett. **67**, 661 (1991).
4. L. Goldenberg and L. Vaidman, Phys. Rev. Lett. **75**, 1239 (1995); quant-ph/9506030.
5. S. N. Molotkov and S. S. Nazin, quant-ph/106046; Pis'ma Zh. Éksp. Teor. Fiz. **73**, 767 (2001) [JETP Lett. **73**, 682 (2001)].
6. A. S. Holevo, Probl. Inf. Transm. **9**, 177 (1973).
7. A. S. Holevo, Usp. Mat. Nauk **53**, 193 (1998).
8. C. E. Shannon, Bell Syst. Tech. J. **27**, 3397 (1948); **27**, 623 (1948).
9. P. Hausladen, R. Jozsa, B. Schumacher, *et al.*, Phys. Rev. A **54**, 1869 (1996).
10. I. M. Gel'fand and N. Ya. Vilenkin, *Generalized Functions*, Vol. 4: *Applications of Harmonic Analysis* (Fizmatgiz, Moscow, 1961; Academic, New York, 1964).
11. N. Wiener and R. Paley, *Fourier Transform in the Complex Domain* (American Mathematical Society, New York, 1934; Nauka, Moscow, 1964).
12. S. N. Molotkov and S. S. Nazin, Zh. Éksp. Teor. Fiz. **121** (6), 1261 (2002) [JETP **94** (6), 1080 (2002)].
13. D. Slepian and H. O. Pollak, Bell Syst. Tech. J. **40**, 40 (1961).
14. W. H. Fuchs, J. Math. Anal. Appl. **9**, 317 (1964).
15. S. N. Molotkov, Pis'ma Zh. Éksp. Teor. Fiz. **74**, 477 (2001) [JETP Lett. **74**, 436 (2001)].

Translated by R. Tyapaev